Received: 16 September 2022 | Revised: 1 June 2023 | Accepted: 2 June 2023

DOI: 10.1002/we.2844

SPECIAL ISSUE PAPER

WILEY

A new coupling of a GPU-resident large-eddy simulation code with a multiphysics wind turbine simulation tool

Emanuel Taschner[1] | Mikko Folkersma[2] | Luis A Martínez-Tossas[3] | Remco Verzijlbergh[2] | Jan-Willem van Wingerden[1]

[1]Delft Center for Systems and Control, Delft University of Technology, Delft, South Holland, Netherlands

[2]Whiffle Weather Forecasting, Delft, South Holland, Netherlands

[3]National Renewable Energy Laboratory, Golden, Colorado, USA

Correspondence
Emanuel Taschner, Delft Center for Systems and Control, Delft University of Technology, Delft, South Holland, Netherlands.
Email: e.taschner@tudelft.nl

Abstract

The development of new wind farm control strategies can benefit from combined analysis of flow dynamics in the farm and the behavior of individual turbines within one simulation environment. In this work, we present such an environment by developing a new coupling between the large-eddy simulation (LES) code GRASP and the multiphysics wind turbine simulation tool OpenFAST via an actuator line model (ALM). In addition, the implementation of the recently proposed filtered actuator line model (FALM) within the coupling is described. The new ALM implementation is cross-verified with results from four other commonly used research LES codes. The results for the blade loads and the near wake obtained with the new coupling are consistent with the other codes. Deviations are observed in the far wake. The results further indicate that the FALM is able to reduce the lift and power overprediction from which the traditional ALM suffers on coarse LES grids. This new simulation environment paves the way for future wind farm simulations under realistic weather conditions by leveraging GRASP's ability to impose data from large-scale meteorological models as boundary conditions.

KEYWORDS
actuator line model, filtered actuator line model, LES simulation

1 | INTRODUCTION

Wind turbines and their aerodynamic behavior have been of great interest for many years.[1,2] However, the turbine is only one part of a large complex dynamical system. This dynamical system possesses spatial scales ranging from the turbine blade boundary layer up to global weather systems and temporal scales spanning from fractions of a second to slow seasonal variations.[3] While the performance of previous turbines could be analyzed in a more isolated state, modern wind turbines are now often clustered in large farms allowing for the generation of wind energy at low cost. The physics of these farms are governed by the flow in the atmospheric boundary layer (ABL), the dynamics of individual turbines and the inherent aerodynamic coupling between turbines due to their wakes.[4,5] The efficient harvesting of the wind resource in these farms requires optimized control algorithms. Control algorithms developed for single turbines aim to increase individual power capture from the incoming wind and to reduce turbine loads.[6] Within the wind farm setting, the control problem is not only limited to the optimization of individual turbine performance but also encompasses the maximization of the overall power capture.[7,8] The interaction of the turbines through their wakes is at the heart of this problem. The wakes, characterized by a velocity deficit and increased turbulence intensity, both reduce the power capture and increase

the loads of turbines located downstream.[4] At the same time, however, wakes also offer an opportunity since existing turbine control degrees of freedom like rotor yaw and blade pitch can be utilized to modify the direction and development of the wakes. New (dynamic) wind farm control algorithms search for yaw and pitch actuation signals, which lead to optimal wake development in terms of power and load distribution across the entire farm.[9–12] Therefore, the successful development of these algorithms relies crucially on the accurate quantification of their impact on the flow as well as the turbine dynamics that motivates the combination of the respective state-of-the-art simulation tools.

State-of-the-art numerical analysis of the flow dynamics in the ABL relies on large-eddy simulation (LES).[13,14] LES solves the filtered Navier–Stokes equations where only the smallest scales of the flow are modeled. It thereby provides insight into a wide range of temporal and spatial turbulent scales.[15] Wind turbines are included in these simulations mostly either via actuator disk models (ADM) or actuator line models (ALM), which both avoid the need for fully blade-resolving meshes.[16,17] However, the ALM captures the footprint of individual turbine blades—in contrast to the ADM—thus enabling the analysis of individual pitch control algorithms.[18] During the last two decades, the ALM has become a prominent method for the representation of wind turbines in LES simulations and has been the subject of continuous development.[19,20] One key component of the ALM is the spreading of the blade forces using a Gaussian kernel of width ϵ. In particular, the choice of the value of ϵ has been the subject of active research. It has been shown that the optimal value for ϵ should be around 25% of the blade's local chord length.[21] However, this finding would imply very fine LES grid resolutions, making the simulation of larger wind farms computationally unfeasible. Simply using coarser grid resolutions and consequently also larger-than-optimal Gaussian spreading leads to the overprediction of blade lift and thus the turbine's power generation. Therefore, corrections were proposed for cases where optimal Gaussian spreading is computationally too restrictive. The choice of correction is an ongoing research topic, and a variety of approaches have been proposed.[22–24] A recently proposed approach is the filtered actuator line model (FALM), which adds a subfilter correction to the LES velocity sampled for the ALM.[25] On the one hand, it was shown that FALM can indeed improve the prediction of lift and power generation for a wind turbine,[26] whereas on the other hand, the impact of the FALM on the wake still needs further research.[27]

The previous outline so far only concerned the analysis of the flow in a wind farm, but as motivated above, the development of new wind farm control algorithms also needs insights into the dynamics of individual wind turbines. These dynamics are analyzed with dedicated multi-physics turbine simulation tools like OpenFAST or HAWC2, which simulate the turbine's aerodynamics, hydrodynamics, the structural dynamics, and the control system.[28,29] In addition, these tools provide a standardized interface for the inclusion of the most recent wind turbine reference controllers.[30] Therefore, the coupling of LES code, a turbine simulation tool, and a turbine controller can provide combined physical insights into the dynamics relevant for the development of the next generation of dynamic wind farm control algorithms. The coupling of OpenFAST and HAWC2 to LES codes has been investigated by several scholars, where, for example, an initial approach by Storey et al. focused on a coupling via an ADM.[31] Later, the feasibility of couplings relying on ALM or actuator sector methods (ASM) was demonstrated, too.[32–35]

The progress in the development of new aero-servo-elastic couplings is accompanied by the growing importance of high-performance computing (HPC) architectures, which employ not only central processing units (CPUs) but also graphical processing units (GPUs). This development also affects the field of LES for wind farms, as it requires the adaption or redesign of codes for optimal usage of the GPU architecture.[36] A very recent example of this trend is the work by Sprague et al,[37] which presented a coupling between OpenFAST and the LES code Nalu-Wind aiming for an effective use of GPUs.

In summary, the development of new dynamic wind farm control strategies asks for a simulation environment that enables the combined analysis of the complex ABL flow-through wind farms and the performance of individual turbines, while ensuring the accuracy of the turbine power predictions also on coarser LES grids. Furthermore, this environment has to be compatible with the next generation of GPU-based HPC architectures. The main contribution of the present study is to develop a new simulation environment that meets these needs by coupling the GPU-resident LES code GRASP (GPU-resident atmospheric simulation platform) with OpenFast via an ALM and the FALM correction. The detailed contributions of this study are as follows:

1. The extensive cross-verification of the new LES-OpenFAST coupling and its FALM correction considering two benchmark cases with reference data from four other research LES codes;
2. An in-depth study of the FALM's impact on a wing and wind turbine rotor and their wakes including the assessment of its convergence behavior and implications for runtime.

The newly established simulation environment hence paves the way for the development of new dynamic wind farm control strategies under realistic weather conditions by leveraging GRASP's ability to impose data from large-scale meteorological models as initial and boundary conditions.

The remainder of this paper is structured as follows. First, an overview of GRASP, the new coupling and its subcomponents including the ALM and FALM implementation, is given in Section 2. Second, Section 3 introduces the three considered wing and wind turbine cases, and Section 4 discusses the results. The cross-verification of the new ALM implementation is documented in Section 4.1. Subsequently, the FALM's impact on rotor and wake is assessed by using a simple translating wing (Section 4.2) and the National Renewable Energy Laboratory (NREL) 5-MW reference wind turbine (Section 4.3). We conclude with a summary and an outlook in Section 5.

2 | THE SIMULATION ENVIRONMENT

The objective of this work is the coupling of the LES code GRASP with the turbine simulation code OpenFAST and the subsequent verification of the coupled simulation environment. The two main codes are described in Sections 2.1 and 2.2. The coupling between the codes is implemented via an ALM or a FALM. The specifics of this coupling are presented in Section 2.3.

2.1 | The LES code: GRASP

The fluid flow is simulated using the LES code GRASP. GRASP solves the filtered three-dimensional Navier–Stokes equations. The core structure of the code is based on the Dutch Atmospheric Large Eddy Simulation model (DALES), which is described in Heus et al.[38] Details about the implementation of DALES on GPUs can be found in Schalkwijk.[39] Furthermore, a proof of concept was delivered with a multi-GPU setup.[40] The GRASP model departs from the DALES formulation as it implements an anelastic approximation.[41] The governing equations for mass and momentum including the anelastic approximation are given by

$$\frac{\partial \rho_b \tilde{u}_j}{\partial x_j} = 0 \tag{1}$$

$$\rho_b \frac{\partial \tilde{u}_i}{\partial t} + \frac{\partial \rho_b \tilde{u}_i \tilde{u}_j}{\partial x_j} = -\frac{\partial \tilde{p}'}{\partial x_i} + \rho_b b \delta_{i3} - \frac{\partial \tau_{ij}}{\partial x_j} + \epsilon_{ij3} f_c (\tilde{u}_j - u_j^g) + f_i^{WT} + f_i^{Fringe} \tag{2}$$

where $i \in \{1,2,3\}$ according to the Einstein summation convention, $\rho_b = \rho_b(x_3)$ is the specified reference density profile, $\tilde{u}_i$ is the filtered velocity, b the buoyancy term $b = -g(\rho'/\rho_b)$ (g being the gravitational constant and $\rho' = \rho - \rho_b$ the density fluctuation), $\tilde{p}'$ is the filtered pressure fluctuation $\tilde{p}' = \tilde{p} - \langle \tilde{p} \rangle$ ($\langle \ldots \rangle$ denotes the horizontal mean), f_c is the Coriolis parameter, u_j^g is the geostrophic wind, f_i^{WT} are the body forces from the wind turbines, f_i^{Fringe} denotes additional forcing terms (e.g., to drive the flow or impose large-scale tendencies), and τ_{ij} is the subgrid-stress tensor. In the following, we use the Cartesian coordinate system $(x_1, x_2, x_3) = (x, y, z)$ when dealing with LES variables, where spatial directions are referred to as streamwise, lateral, and vertical, respectively.

Using the symmetric part of the resolved velocity gradient tensor $\tilde{S}_{ij} = 0.5(\partial \tilde{u}_i/\partial x_j + \partial \tilde{u}_j/\partial x_i)$, the subgrid-stress tensor can be written as

$$\tau_{ij} = -\rho_b K_m \left(\frac{\partial \tilde{u}_i}{\partial x_j} + \frac{\partial \tilde{u}_j}{\partial x_i} \right) = -2 \rho_b K_m \tilde{S}_{ij} \tag{3}$$

In this study, the eddy viscosity K_m is modeled using the Smagorinsky subgrid model

$$K_m = (C_s \Delta)^2 \sqrt{2 \tilde{S}_{ij} \tilde{S}_{ij}} \tag{4}$$

where C_s is the Smagorinsky constant and the subgrid filter scale is denoted as $\Delta = (\Delta_x \Delta_y \Delta_z)^{1/3}$.[42] For the remainder of this article, we omit the tilde sign for filtered variables for convenience. Spatial discretization in GRASP uses the Arakawa C-grid, which is a spatially staggered grid. The cell centers and cell faces are referred to as full and half levels, respectively. All prognostic variables reside on the cell center except the three velocity components. For example, consider the direction $i = 1$. The velocity component u_x resides on the half level of the grid in the x direction, whereas it is located on the full levels in the remaining two directions, y and z. The advection scheme uses second-order central differences.[38] The time stepping can be done both with variable and fixed time step value Δt. A third-order Runge–Kutta scheme is used for explicit time integration of the governing equations.[43] Due to the periodicity of the streamwise and lateral directions, a pressure solver based on a fast Fourier transform can be employed, which acts on the periodic pressure fluctuation field $\tilde{p}'$. It ensures that the continuity equation is satisfied by computing the corresponding pressure fluctuations.

The main application of the LES code is for both weather hindcasting and operational forecasting. For example, Gilbert et al[44] delivered a proof of concept using Grasp for operational forecasting at the Horns Rev I wind farm site. An application of GRASP for hindcasting purposes is presented in Schepers et al.[45] They carried out a year-long hindcasting LES simulation with GRASP in order to study the effect of extreme events on the aero-elastic loads of a 10-MW wind turbine. Both of these studies use LES with periodic horizontal boundary conditions forced with tendencies from large-scale weather models. This approach requires additional source terms in Equation (2) representing large-scale subsidence, large-scale pressure gradients (expressed as geostrophic wind), large-scale advective tendencies, and a relaxation term to avoid model drift (for details see Schalkwijk et al.[46]). GRASP enables the simulation of multiple nested LES domains in parallel where the solution of an outer domain

forces the subsequent inner domain and only the most inner domain contains the wind turbines. As a consequence, the simulation of wind farms using periodic boundary conditions and large-scale forcing is enabled but avoids the recirculation of the turbine wakes which would occur when using a single periodic domain.[47] Other large-scale forcing approaches in literature avoided the assumption of horizontal homogeneity made for GRASP by not relying on periodic boundary conditions, however, in doing so also limiting the range of permitted wind directions.[48]

2.2 | OpenFAST

The wind turbine dynamics are simulated using the open-source tool OpenFAST developed by the NREL, USA.[28,49] OpenFAST follows a modular modeling approach where each module calculates a part of the turbine dynamics. The different modules include aerodynamics, hydrodynamics, control, and structural dynamics. The overarching OpenFAST glue code manages the coupling of the modules and enables the integrated simulation of nonlinear aero-hydro-servo-elastic wind turbine dynamics. OpenFAST also offers a C++ application programming interface (API) in order to link it to external programs. In this work, we utilize this API to develop a coupling between OpenFAST and the LES code GRASP. In addition, the present study employs the following physics modules of OpenFAST:

1. AeroDyn: It calculates the aerodynamic loading of the wind turbine. The blades and tower are discretized using analysis nodes spread along actuator lines. AeroDyn is provided by OpenFAST with the instantaneous orientation, position, and flow velocity for each analysis node. Blade element theory relying on two-dimensional airfoil data is then used to calculate the local drag force, lift force, and pitching moment.
2. ElastoDyn: It calculates the structural dynamics of the turbine. The turbine's desired degrees of freedom for blades, tower, generator, and nacelle are set in this module. ElastoDyn receives the aerodynamic loads and controller commands as input. Based on this input, the resulting displacements, structural velocities/accelerations, and reaction loads are calculated.
3. ServoDyn: This module covers all control aspects of the turbine including pitch, generator/torque, and yaw control. In addition, ServoDyn offers a bladed-style DISCON controller interface. This interface allows for a simple integration of external turbine controllers.

2.3 | The LES-OpenFAST coupling

This section describes the newly developed coupling between GRASP and OpenFAST. GRASP calculations are carried out on the GPU, but through its API ASPIRE, it is possible to couple plugins running on CPUs. The coupling is realized with a new ASPIRE plugin written in C++, which is called AspFAST. AspFAST tasks are to synchronize the LES and OpenFAST simulations, to exchange information between the two main codes (forces, velocity, turbine blade position/orientation) and to perform the calculations for the ALM/FALM that are not covered by OpenFAST. A schematic of the resulting simulation environment is shown in Figure 1. It is important to note that in OpenFAST the blade is discretized with both N_F force actuator and N_V velocity actuator points, where in general $N_F \neq N_V$. The number of points N_F is flexible and is specified in AspFAST. The number of points N_V, on the other hand, is determined by the number of blade stations which are set in the AeroDyn blade specification file. An increase in velocity actuator points thus requires the interpolation of the initial blade input data to the desired value of N_V points. The outline of the ALM and FALM below uses the following notation for the discretized solution. The subscript $(\ldots)_i$ still refers to the Einstein summation convention denoting the spatial direction with respect to the corresponding coordinate system. In addition, we introduce the superscripts x^k and x^q to denote the k^{th} force and q^{th} velocity actuator point, respectively. The discrete solution at time step t^n is indicated with the superscript $(\ldots)^n$.

During initialization, the user input data (number of turbines, turbine positions, N_F) are read by AspFAST and communicated to OpenFAST. At each subsequent time step t^n, AspFAST receives the full LES velocity field $u_i^n(x_i)$ from GRASP and the current blade point positions x_i^k and x_i^q from

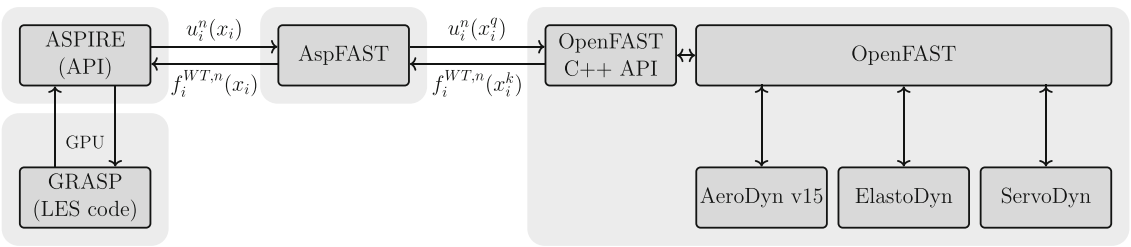

FIGURE 1 Schematic of the new simulation environment. The ASPIRE plugin AspFAST manages the communication between the large-eddy simulation (LES) code and the OpenFAST C++ API at each time step t^n. In addition, it implements the sampling of the LES velocity at the actuator points, the projection of the point forces back to the LES grid, and optionally the calculation of the filtered actuator line model (FALM) correction.

OpenFAST. The LES velocity at the current velocity actuator point $u_i^n(x_i^q)$ is sampled using linear interpolation from the nearest LES grid point x_i and then sent to OpenFAST. Provided with the LES velocity input, OpenFAST advances the turbine model by one time step. In a minimum configuration, this step entails the calculation of the aerodynamic loads by AeroDyn and the update of the actuator point locations. Note that the wake/induction model in AeroDyn is disabled since these effects are resolved by the LES. In particular, AeroDyn calculates the spanwise distribution of the aerodynamic forces acting on the blade using blade element theory based on two-dimensional airfoil look-up tables for drag and lift coefficients.[50] Using the local velocity magnitude,

$$U_{Rel}^n(x_i^q) = \sqrt{\left(u_{ax}^n(x_i^q)\right)^2 + \left(\Omega^n r^q - u_\theta^n(x_i^q)\right)^2} \tag{5}$$

the local inflow angle at each blade element can be determined as

$$\phi^n(x_i^q) = \tan^{-1}\left(\frac{u_{ax}^n(x_i^q)}{\Omega^n r^q - u_\theta^n(x_i^q)}\right) \tag{6}$$

where the velocities are expressed in a blade-aligned coordinate system $(x_1, x_2, x_3) = (r, \theta, ax)$. Ω denotes the rotor speed. The local angle of attack is obtained by subtracting the sum of the local twist angle and the blade pitch angle (their sum is denoted as γ)

$$\alpha^n(x_i^q) = \phi^n(x_i^q) - \gamma^n(x_i^q) \tag{7}$$

The local lift and drag forces are then obtained utilizing the airfoil look-up tables for lift coefficient $C_L = C_L(\alpha, Re)$ and drag coefficient $C_D = C_D(\alpha, Re)$ dependent on Reynolds number Re and angle of attack

$$\frac{F_L^n(x_i^q)}{\Delta r(x_i^q)} = \frac{1}{2}\rho\left(U_{Rel}^n(x_i^q)\right)^2 c(x_i^q) C_L^n(x_i^q) \tag{8}$$

$$\frac{F_D^n(x_i^q)}{\Delta r(x_i^q)} = \frac{1}{2}\rho\left(U_{Rel}^n(x_i^q)\right)^2 c(x_i^q) C_D^n(x_i^q) \tag{9}$$

where the density ρ is specified in the AeroDyn input file, $\Delta r(x_i^q)$ denotes the spanwise extent of the blade element associated with the actuator point, and c is the local chord length. The resultant force vector is transformed back into the Cartesian LES coordinate system and communicated to AspFAST at the force actuator point locations x_i^k. This point force $f_i^{WT,n}(x_i^k)$ is spread across multiple LES grid points using a convolution with a constant Gaussian kernel η_ϵ with kernel width ϵ

$$\eta_\epsilon = \frac{1}{\epsilon^3 \pi^{3/2}} \exp\left(\frac{-(x_i - x_i^k)^2}{\epsilon^2}\right) \tag{10}$$

$$f_i^{WT,n}(x_i) = f_i^{WT,n}(x_i^k) \bigotimes \eta_\epsilon \tag{11}$$

thereby ensuring that singular behavior is avoided and the resulting force distribution is smooth. The resultant body force distribution $f_i^{WT,n}$ is then applied as additional force term in the flow domain (i.e., in Equation 2). The ALM as outlined above follows the traditional ALM formulation as developed by Sorensen and Shen.[18] As outlined in Section 1, the ALM in its traditional form suffers from overpredicted blade torque and thus power generation if the Gaussian kernel width is chosen larger than the value found to be optimal $\epsilon > \epsilon^{Opt}$. However, the requirement for the optimal value of the Gaussian kernel is very restrictive since it leads to very fine grid resolutions, which are infeasible for LES simulations on wind farm scale. Therefore, Martínez-Tossas and Meneveau[25] proposed a subfilter correction applied to the sampled LES velocity. This method labeled as FALM aims to remedy the issue of torque overprediction for cases where $\epsilon > \epsilon^{Opt}$. In the following, the formulation of FALM and its implementation in the LES-OpenFAST coupling are described.

For the implementation in AspFAST, forces and velocities are kept in vector form throughout the calculation; thus, the same is done for the outline of the equations below. The usage of $\epsilon > \epsilon^{Opt}$ for LES leads to the underestimation of induced velocity. This reduced strength of the induced velocity causes larger angles of attacks along the blade than would have occurred with ϵ^{Opt}. The main idea of FALM is to determine the resolved and the missing part of the induced velocity in order to correct the sampled LES velocity for the effect of a suboptimal kernel size ϵ^{LES}

$$\hat{u}_i(x_i) = u_i(x_i) + \left[u_{i,ind}(x_i; \epsilon^{Opt}) - u_{i,ind}(x_i; \epsilon^{LES})\right] \tag{12}$$

The numerical procedure to obtain this subfilter correction can be summarized as follows. The calculation of the correction requires the knowledge of the freestream velocity excluding the effects of induced velocity. This velocity can be approximated as follows:

$$U^n_{i,\infty}(x^k_i) = u^n_i(x^k_i) - u^n_{i,ind}(x^k_i;\epsilon^{LES}) \tag{13}$$

The lift force at each blade element acts perpendicular to $U^n_{i,\infty}(x^k_i)$. Since OpenFAST only returns the resultant force vector, the lift force is not directly available. However, the lift force can be recovered using the local unperturbed inflow velocity

$$G^{n-1}_i(x^k_i) = \frac{1}{2}c(x^k_i)C_L(x^k_i)U_{j,\infty}(x^k_i)U_{j,\infty}(x^k_i) = \frac{1}{\rho\Delta x^k}\left(f^{WT,n-1}_i(x^k_i) - U_{i,\infty}(x^k_i)\frac{f^{WT,n-1}_j(x^k_i)U_{j,\infty}(x^k_i)}{U_{j,\infty}(x^k_i)U_{j,\infty}(x^k_i)}\right) \tag{14}$$

Furthermore, the gradient of G^{n-1}_i along the blade span is obtained using finite differences

$$k = 1:\ \Delta G^{n-1}_i(x^1_i) = G^{n-1}_i(x^1_i) \tag{15}$$

$$k \in (2, N_F - 1):\ \Delta G^{n-1}_i(x^k_i) = \frac{1}{2}[G^{n-1}_i(x^{k+1}_i) - G^{n-1}_i(x^{k-1}_i)] \tag{16}$$

$$k = N_F:\ \Delta G^{n-1}_i(x^1_i) = -G^{n-1}_i(x^{N_F}_i) \tag{17}$$

Using the lift gradient, one can then calculate the resulting induced velocity at the k^{th} actuator point for a given kernel width ϵ:

$$u^n_{i,ind}(x^k_i;\epsilon) \approx -\sum_{l=1}^{N_F}\frac{1}{\sqrt{U_{j,\infty}(x^l_i)U_{j,\infty}(x^l_i)}}\frac{1}{4\pi(x^k_i - x^l_i)}\Delta G^{n-1}_i(x^l_i)\left(1 - \exp\left(\frac{-(x^k_i - x^l_i)^2}{\epsilon^2}\right)\right) \tag{18}$$

At each time step, Equation (18) is evaluated twice per actuator point. The first evaluation uses the kernel size $\epsilon = \epsilon^{LES}$ to obtain the part of the induced velocity which is already resolved by the LES. The second evaluation sets $\epsilon = \epsilon^{Opt}$, which results in the induced velocity which would have been observed in a highly resolved ALM-LES simulation allowing for $\epsilon^{LES} = \epsilon^{Opt}$. Finally, under-relaxation is applied to determine the updated subfilter velocity correction accounting for the difference in resolved and optimal-induced velocity

$$\Delta u^n_{i,ind}(x^k_i) = f_u[u^n_{i,ind}(x^k_i;\epsilon^{Opt}) - u^n_{i,ind}(x^k_i;\epsilon^{LES})] + (1 - f_u)[u^{n-1}_{i,ind}(x^k_i;\epsilon^{Opt}) - u^{n-1}_{i,ind}(x^k_i;\epsilon^{LES})] \tag{19}$$

which is added to the sampled LES velocity:

$$\hat{u}^n_i(x^k_i) = u^n_i(x^k_i) + \Delta u^n_{i,ind}(x^k_i) \tag{20}$$

A factor $f_u = 0.1$ is recommended for the under-relaxation.[25] It is noted that AspFAST receives the force vectors from OpenFAST always at the force actuator points. Therefore, the entire FALM calculations are carried out at the force actuator point locations, and only the final corrected LES velocities are interpolated to the velocity actuator points before they are sent to OpenFAST. The entire coupling algorithm with the optional application of the FALM is shown in Algorithm 1 in Appendix A.

3 | CASE SETUP OF THE NUMERICAL SIMULATIONS

The new simulation environment is employed to study a total of three cases. The first case serves the objective of cross-verifying the ALM implementation with four other popular research LES codes (Section 3.1). The remaining two cases concern the objective of testing the FALM implementation and assessing its performance compared with the ALM. In the second case, the FALM is applied to a translating constant chord wing (Section 3.2), whereas in Section 3.3, the FALM is applied to the NREL 5-MW reference wind turbine. For both turbine cases, the focus is on modeling the rotor since the reference data in Section 3.1 only include the rotor forces and the aim in Section 3.3 is to study the impact of the FALM on the rotor performance in isolation. Modeling the tower and nacelle with an immersed boundary method[51] or including the nacelle by means of an anisotropic Gaussian body force[52] would further improve the accuracy of especially the near wake predictions. All cases use uniform inflow with a specified reference velocity $u^{ref}_i = (U_\infty, 0, 0)$. The boundary conditions in the streamwise and lateral direction are periodic. In order to

ensure an uniform inflow with the desired reference velocity, a fringe region is included in the inlet/outlet region of the domain. Within the fringe region, an additional source term is added to the momentum equations, which drives the flow again toward u_i^{ref}:

$$f_i^{Fringe} = \rho_b \left(\frac{\partial u_i}{\partial t}\right)^{Fringe} = -\rho_b \frac{\alpha(x,y,z)\eta}{\Delta t}(u_i - u_i^{ref}) \tag{21}$$

The strength of the forcing is controlled with the fringe factor η. The relaxation strength $\alpha(x,y,z)\eta/\Delta t$ is an inverse time scale, where α is a weighting function varying from a value of one at the inlet/outlet to a value of zero at the boundary of the fringe region according to a second-order polynomial. The maximum fringe strength and extent are chosen as small as possible while still ensuring that the uniform inflow profile is recovered. The top boundary condition (BC) at $z = L_z$ enforces a vanishing vertical velocity component and vanishing gradient for the streamwise and lateral velocity components. The bottom boundary condition (at $z = 0$) in GRASP is currently only designed for the simulation of the ABL; thus, it does not offer a zero-shear-stress bottom BC, yet. For the purpose of this study, an approximately zero-friction velocity u^* is specified for the surface scheme of the bottom BC. This approach achieves in combination with the relatively coarse grid resolution that there is no boundary layer forming above the bottom boundary surface. The constraint is kept in mind for the analysis of the wake results. The chosen time step for all simulations ensures that the local Courant–Friedrich–Levy number (CFL) is kept below a value of one.[19]

3.1 | ALM: Cross-verification

The implementation of the new coupling is cross-verified by performing an ALM simulation of a popular reference case, which has been already used previously to compare four research LES codes and their ALM implementation.[53] This case considers a single NREL 5-MW turbine[54] ($D = 126$m) which is placed in a uniform laminar inflow of $U_\infty = 8$m/s. The turbine blades are considered as rigid, and the rotational speed of the rotor is set to a constant value of $\Omega = 9.155$rpm. At this set point, the turbine is operating at its optimal power coefficient. The density is set to $\rho = 1\text{kg/m}^3$. The tilt angle of the rotor is set to zero in the OpenFAST model of the turbine in order to ensure a streamwise aligned wake. As noted in Martínez et al,[53] there are two different approaches on how to obtain the blade specifications for the actuator points located between the last defined point of the NREL 5-MW turbine and the tip of the blade. Data can be either extrapolated from the last two defined data points or interpolated based on a zero chord assumption at the tip of the blade. For the present case, the latter approach is chosen, whereas the former approach is applied in Section 3.3, demonstrating the impact of this choice.

Initial tests with a streamwise domain length equal to the reference case ($L_x = 24$D) showed that the forcing of the fringe region influenced the wake recovery. Therefore, the GRASP domain is extended by a factor of approximately two compared with the reference case in order to account for the length and the influence of the fringe region at the domain outflow. The coefficient for the Smagorinsky subgrid model is chosen as $C_s = 0.16$ to be consistent with the reference. For a summary of the simulation parameters, see Table 1. It is noted that the chosen resolution of the reference case cannot be exactly reproduced due to current limitations of maximum available GPU memory (using one NVIDIA A100 40GB GPU).

3.2 | FALM: Translating wing test case

The implementation of the FALM is first tested for a translating wing under uniform inflow. This case was already used in previous studies for the testing of the FALM[25,26] and the development of an ALM tip correction.[22] A constant chord wing is placed inside the domain centered with respect to all three axes. The spanwise direction of the wing is parallel to the y-axis. The angle of attack is $\alpha = 6^\circ$. The airfoil is of type NACA64A17, which is also used for the most outer part of the blade of the NREL 5-MW turbine. The objective is to simulate these case specifications with an unmodified version of the newly developed LES-OpenFAST coupling. To this end, the OpenFast model of the NREL 5-MW turbine is simplified to represent the single constant chord wing. In particular, the number of blades is reduced to one, the AeroDyn blade input file is modified to contain only the NACA64A17 airfoil type along the entire span of the wing, the rotor speed is set to zero, and azimuth/pitch angles are adjusted to ensure the desired angle of attack $\alpha = 6^\circ$ with respect to the incoming flow. The employed subgrid model is the standard

TABLE 1 Parameter settings for the ALM cross-verification case including the hub position of the turbine $L_{x,Hub}, L_{y,Hub}, L_{z,Hub}$; the domain size $L_x \times L_y \times L_z$; the number of actuator points for force and velocity nodes N_F/N_V; the nondimensional spreading ϵ/D; grid resolution $\epsilon/\Delta x$; and simulation time $T_{Sim}U_\infty/L_x$.

$L_{x,Hub}, L_{y,Hub}, L_{z,Hub}$	$L_x \times L_y \times L_z$	N_F	N_V	ϵ/D	$\epsilon/\Delta x$	$T_{Sim}U_\infty/L_x$
4.5D, 3D, 3D	53.25D × 6D × 6D	64	19	0.079	3.39	≈ 2

Smagorinski model with $C_S = 0.16$. The effect of the subgrid model was found to be not crucial for this test case.[25] Calculations are carried out with the ALM and FALM for three different spreading parameters ϵ/c and two different grid resolutions $\epsilon/\Delta x$. In total, this results in a set of 12 simulations (see Table 2).

3.3 | FALM versus ALM: NREL 5-MW turbine

After cross-verifying the basic ALM for the NREL 5-MW turbine and the FALM for the translating wing, the study concludes with a performance comparison of the ALM and FALM applied to the NREL 5-MW turbine. The case setup is identical to the one presented in Section 3.1. In total, four simulations are performed considering two different choices of the Gaussian spreading parameter for both ALM and FALM. The chosen values of the Gaussian spreading are typical for the simulation of a wind farm using LES/ALM on a coarse grid and therefore allow the quantification of the dependence of ALM and FALM results on ϵ in these practical use cases. The setup maintains a ratio of $\epsilon/\Delta x \approx 3$ and a constant grid spacing in x, y, and z. This results in slightly different streamwise domain lengths L_x since the number of grid points in GRASP has to be an integer multiple of 32. The chosen resolution is a trade-off between the available computational resources for practical applications of the ALM on wind farm scale and the full convergence of the results. It fulfills the requirement $\epsilon/\Delta x > 2$ in order to avoid numerical oscillations[19] but is below the ratio of $\epsilon/\Delta x = 5$, which has been found necessary for fully converged results.[55] Compared with the initial ALM simulations, the number of actuator points has to be significantly increased when using the FALM. Only then are the large lift gradients at the blade tip resolved, which are crucial for the calculation of the FALM correction term. A summary of the parameter settings for this case is shown in Table 3.

4 | RESULTS

This section presents the results obtained with the GRASP-OpenFAST coupling for the test and verification cases presented in Section 3. Firstly, the results of the ALM cross-verification are shown in Section 4.1. Secondly, the FALM verification using the translating wing test case is presented in Section 4.2. We conclude with the comparison of the FALM and ALM performance in Section 4.3. For the performance assessment of the new simulation environment, it is referred to Appendix B.

4.1 | ALM: Cross-verification

The new coupling of GRASP and OpenFAST via an ALM is cross-verified by comparing the predictions for the NREL 5-MW reference turbine in uniform inflow to the ALM results of four other research LES codes. The codes considered for the comparison are LESGO (Johns Hopkins University: JHU), SOWFA (NREL), SP-Wind (KU Leuven: KUL), and EllipSys3D (Technical University of Denmark: DTU). The codes are compared in terms of predictions for the blade and wake quantities. Temporal averaging of the results of the four reference codes is done for one to two flow-through times T_F, excluding the initial flow-through time during which the flow develops. For GRASP, it is found that the initial transient development takes slightly longer than $T_F = 1$, and averaging is done across an interval of $1.85T_F$ starting at $t_{Sim} = 1.3T_F$, where T_F is calculated with the streamwise length of the reference case ($L_x = 24$D) and not the extended GRASP domain. As mentioned previously, it is found that the location of the laminar-turbulent transition in the wake and its recovery in GRASP are sensitive to the strength of the fringe in the outflow region. However, even for very weak fringe forcing, mean quantities in the far wake are modified as soon as the initially created wake reaches the outflow

TABLE 2 Parameter settings for the translating wing test case, including the wing span S, the domain size $L_x \times L_y \times L_z$, the number of actuator points for force and velocity nodes N_F/N_V, the non-dimensional spreading ϵ/c, grid resolution $\epsilon/\Delta x$, and simulation time $T_{Sim}U_\infty/L_x$.

S	$L_x \times L_y \times L_z$	N_F	N_V	ϵ/c	$\epsilon/\Delta x$	$T_{Sim}U_\infty/L_x$
12.5c	2.5S × 2.5S × 2.5S	300	100	{1;2;4}	{4;8}	3.2

TABLE 3 Parameter settings for the ALM cross-verification case, including the hub position of the turbine $L_{x,Hub}, L_{y,Hub}, L_{z,Hub}$; the domain size $L_x \times L_y \times L_z$; the number of actuator points for force and velocity nodes N_F/N_V; the nondimensional spreading ϵ/D, grid resolution $\epsilon/\Delta x$; and simulation time $T_{Sim}U_\infty/L_x$.

$L_{x,Hub}, L_{y,Hub}, L_{z,Hub}$	$L_x \times L_y \times L_z$	N_F	N_V	ϵ/D	$\epsilon/\Delta x$	$T_{Sim}U_\infty/L_x$
4.5D, 3D, 3D	{53.1; 52.8}D × 6D × 6D	307	307	{0.079;0.11}	≈3	≈2

Abbreviations: ALM, actuator line model.

boundary. In the present study, this influence is mitigated by choosing a very long domain length of $L_x = 53.25D$, which allows for a sufficiently long averaging interval before the initial wake interacts with the fringe forcing.

The five ALM implementations are first compared in terms of their predictions for mean quantities along the spanwise direction of the blade. The mean distributions of angle of attack $\bar{\alpha}$, axial velocity $\bar{u}_x/U_\infty$, and drag/lift force are shown in Figure 2, where forces are nondimensionalized with the rotor diameter D, the fluid density ρ, the inflow wind speed U_∞, and the spanwise width Δr of the respective blade segment. The four reference LES codes show overall similar distributions for angle of attack and drag/lift forces. However, the previous study of Martínez-Tossas et al,[53] which compared the four reference ALM implementations, also pointed out two main reasons for deviations between the results. The first one is the treatment of the actuator points close to the tip of the blade, whereas the second one concerns the treatment of the transitions between different airfoil types along the blade. The GRASP results are obtained from OpenFAST at the N_V velocity actuator point locations, where the most outer specified point in the AeroDyn blade input file is located precisely at the blade tip. The specifications for this actuator point are not uniquely defined since the last documented point of the NREL 5-MW turbine is located further inward. For this comparison, the assumption of vanishing chord length at the blade tip is used. As a consequence, the drag and lift distributions obtained with GRASP tend toward zero at $r = R$. The second possible choice of extrapolating the chord length specified for the most outer actuator point from the two neighboring inner points is demonstrated later in Section 4.3. The second cause of deviations (especially for the axial velocity profile) is the possibility to interpolate the drag and lift tables when the airfoil type is changed in between two blade sections. This approach is only implemented in the EllipSys3D code, which thereby obtains smooth distributions along the blade. The remaining four codes show discontinuities at locations where the airfoil type changes. It should be noted that the GRASP-OpenFAST coupling uses $N_F = 64$ force actuator points as the other four codes, but in fact, the shown blade quantities are obtained at the $N_V = 19$ velocity actuator points, thus leading to coarser profiles. The blade quantities nevertheless show good agreement with the four references. The only exception is the nonresolved peak of the drag force near $r/R = 0.175$. The second notable deviation of the GRASP results is the prediction of smaller axial velocities $\bar{u}_x/U_\infty$ compared with the other three codes, which choose to not interpolate in between airfoil types. This deviation is most likely due to the fact that the GRASP simulation only reaches a resolution of $\epsilon/\Delta x \approx 3.39$, which is limited by the size of the GPU memory, whereas the references use $\epsilon/\Delta x \approx 5$. Additional tests with smaller domains but refined grids show that the GRASP solution shifts toward the three references.

The small differences in the implementation of the ALM also have an effect on the wake. In Figures 3 and 4, velocity $\bar{u}_x(z)/U_\infty$ and streamwise Reynolds stress $\overline{u_x'u_x'}(z)/U_\infty^2$ profiles are shown at seven locations downstream of the turbine. The former quantity is of main concern

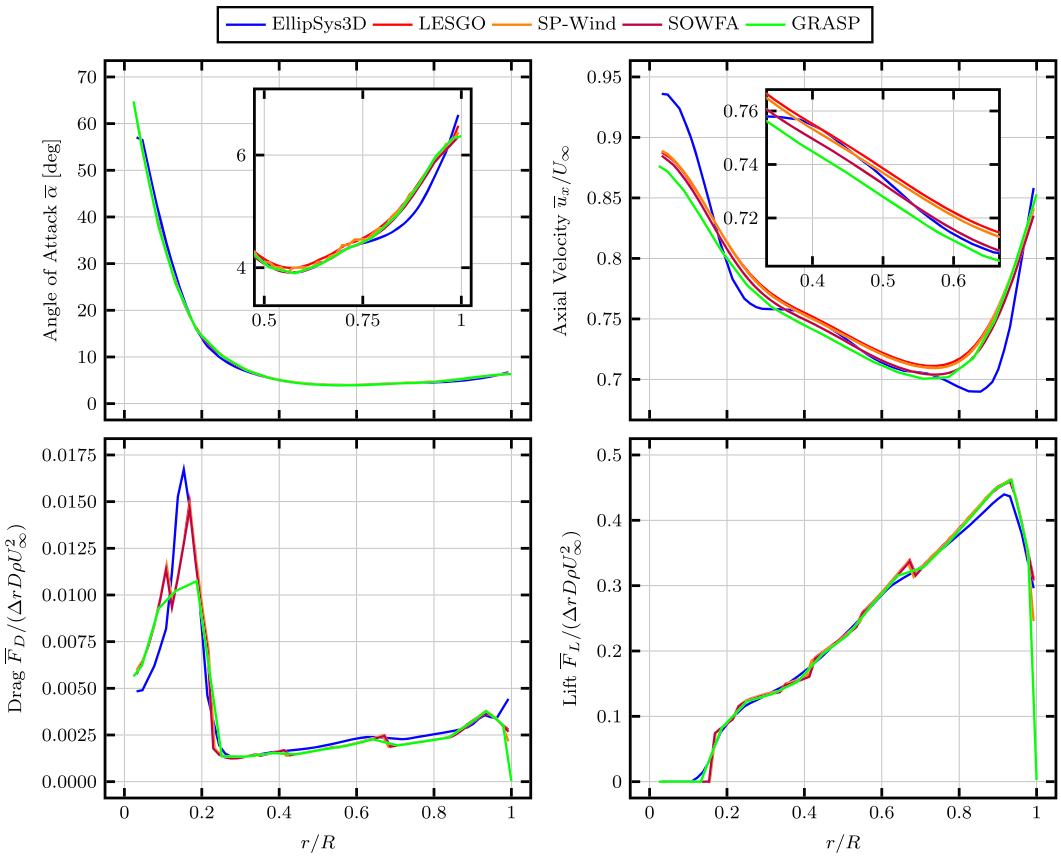

FIGURE 2 Comparison of mean angle of attack $\bar{\alpha}$, axial velocity $\bar{u}_x/U_\infty$, drag, and lift per unit length along the blade span.

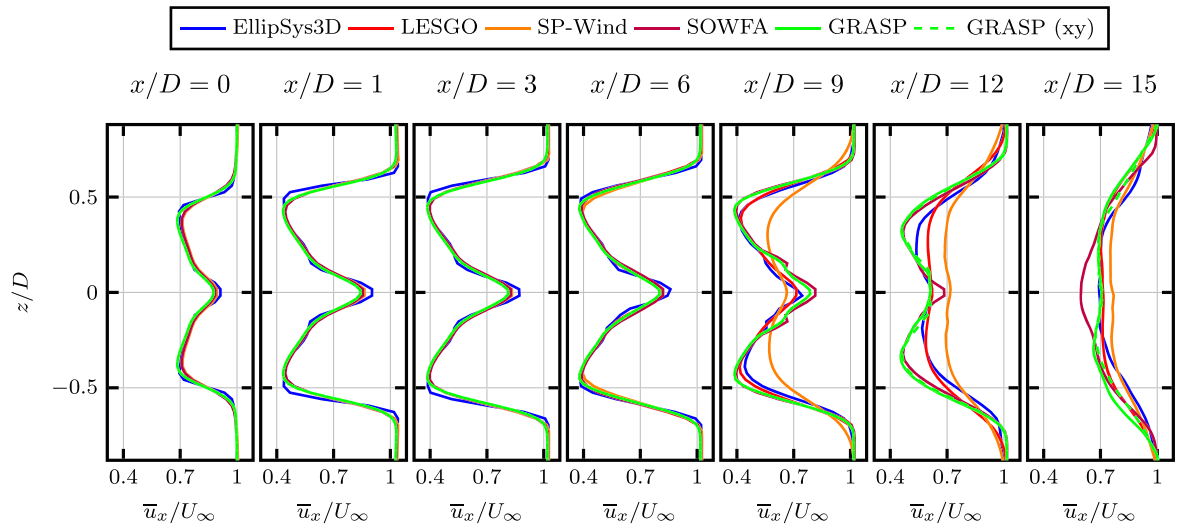

FIGURE 3 Comparison of mean streamwise velocity profiles $\bar{u}_x/U_\infty$ at seven locations in the wake downstream of the turbine. For GRASP, the profiles in lateral direction (labeled xy) are shown in addition to the vertical profiles.

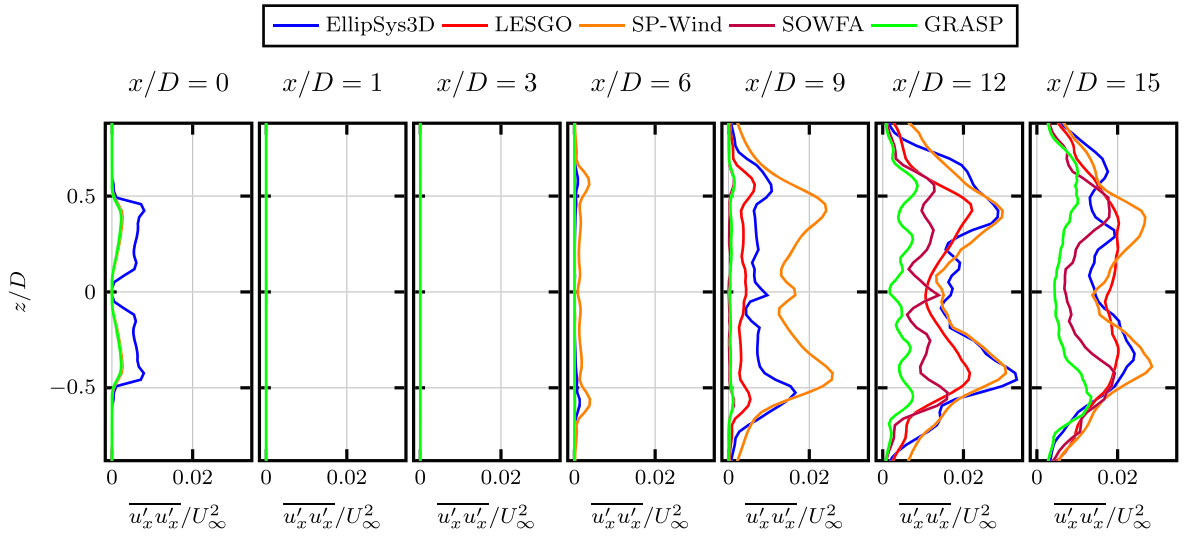

FIGURE 4 Comparison of streamwise Reynolds stress profiles $\overline{u'_x u'_x}/U_\infty^2$ at seven locations in the wake downstream of the turbine.

for the power production of a hypothetical downstream turbine, whereas the latter one indicates the onset of transition in the wake. The codes predict similar velocity profiles for the laminar region of the wake $x/D \approx (0,6)$. The only exception is the EllipSys3D code, which already shows a stronger shear layer gradient in the rotor plane. This stronger gradient persists in the near wake region and causes the wake to transition earlier than the other two second-order finite difference codes SOWFA and GRASP (see locations $x/D = \{9;12\}$). The two remaining codes (LESGO and SP-Wind) use pseudo-spectral discretization for the horizontal directions, which leads to the earlier onset of laminar-turbulent transition and faster recovery of the wakes.[53] These differences become less pronounced far downstream ($x/D = 15$) when the wakes are turbulent for all codes. In the turbulent far wake at $x/D = 15$, the vertical velocity profile calculated by GRASP shows a slight asymmetry with respect to the center axis of the wake. This asymmetry is not present for the velocity profile in the lateral direction (shown as reference in Figure 3 with a dashed green line) and is likely to be caused by the fact that GRASP currently does not offer a zero shear stress (slip wall) BC for the bottom boundary as explained in Section 3. To confirm this hypothesis, future testing with newly implemented BCs for the vertical direction is necessary.

An overall comparison of the wake structure is facilitated by analyzing two-dimensional contours of the mean streamwise velocity and Reynolds stress in a vertical *x*-*z* plane (see Figures 5 and 6, respectively). The Reynolds stress magnitude clearly indicates that transition is triggered the earliest in SP-Wind ($x/D \approx 5.5$), followed by EllipSys3D and LESGO. For both SOWFA and GRASP, the onset of transition is the furthest downstream at $x/D \approx 10$. GRASP uses a spatially staggered grid, which improves the accuracy of the second-order finite difference discretization

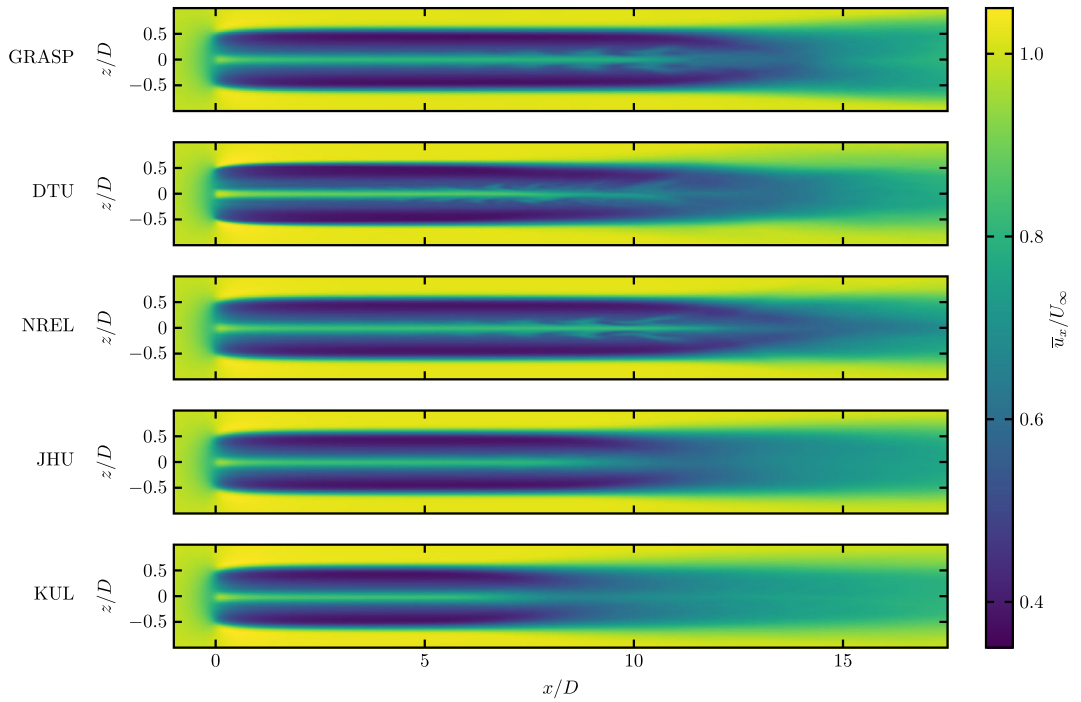

FIGURE 5 Comparison of mean streamwise velocity contours $\bar{u}_x/U_\infty$ for the five large-eddy simulation (LES) codes. The rotor is located at $x/D = 0$.

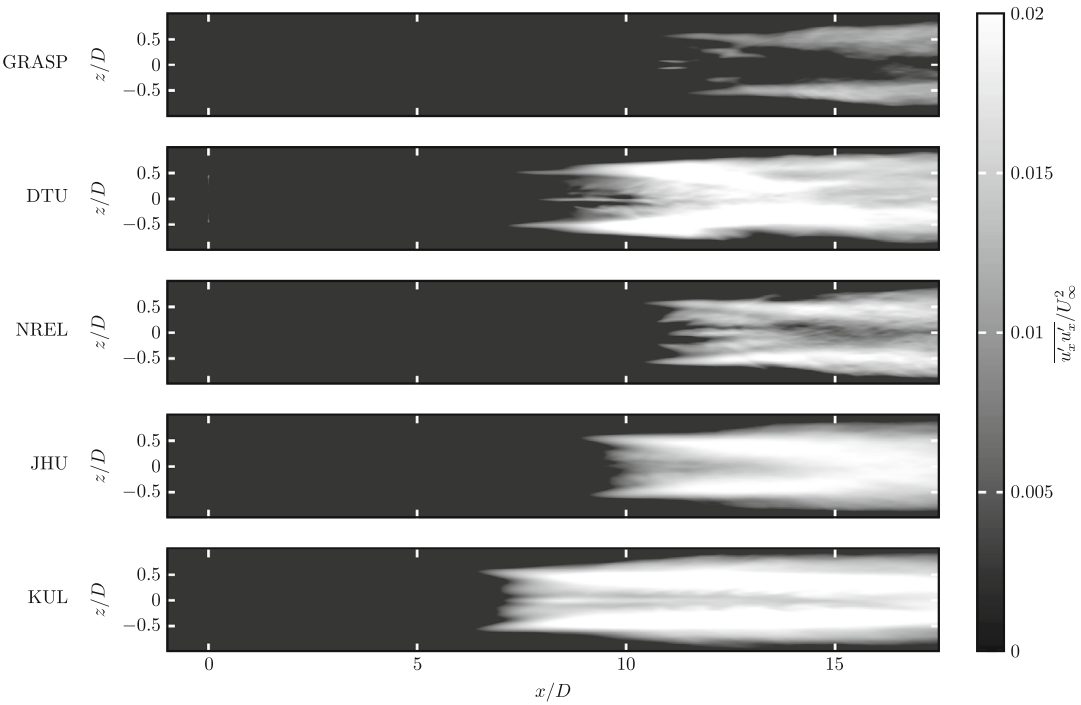

FIGURE 6 Comparison of streamwise Reynolds stress contours $\overline{u'_x u'_x}/U_\infty^2$ for the five large-eddy simulation (LES) codes. The rotor is located at $x/D = 0$.

compared with the collocated grid arrangement employed in SOWFA.[56] Consequently, one would expect the onset of turbulence to occur earlier for GRASP since high wave number modes, which trigger turbulence, are less damped.[53] However, as discussed previously, the present GRASP study can only achieve a resolution of $\epsilon/\Delta x \approx 3.39$; therefore, the gain in accuracy achieved by the grid arrangement is again lost due to the coarser grid resolution. This current limitation also affects the magnitude of the Reynolds stress predicted by GRASP, which is smaller throughout the wake. Multi-GPU parallelization of GRASP is currently under development and will enable future comparisons with finer grid resolutions.

4.2 | FALM: Translating wing test case

In addition to the introduced ALM implementation, the GRASP-OpenFAST coupling also offers a FALM extension that can improve the ALM performance on coarse grids. The implementation of the FALM is first tested using a translating wing in uniform inflow before applying it to an entire wind turbine rotor (see Section 3.2 for a description of the case setup). The resulting flow field forming around the wing is shown in Figure 7A. The vorticity magnitude displays the typical horseshoe shape associated with the bound circulation along the wing span and the shed vorticity at the tips of the finite-span constant chord wing. The contour of vertical velocity clearly indicates the regions of upwash and downwash present in the proximity of the wing and in its wake. Figure 7B,C shows a comparison of ALM and FALM results for the streamwise vorticity ω_x and lateral vorticity ω_y at the wing location $x/S = 0$ where the bound vortex ω_y is located and in the wake at $x/S = 0.25$ where only the tip vortices ω_x remain. It is important to note that there are only minor differences between the two models since also the FALM uses the same coarse ϵ to project the actuator point forces onto the LES grid. The FALM thus mainly affects the local quantities along the wing (like induced velocity and lift) on which we focus in the following.

The wing is simulated using both ALM and FALM for a set of different kernel widths $\epsilon/c = \{1;2;4\}$ and grid resolutions $\epsilon/\Delta x = \{4;8\}$. The reference study of Martínez-Tossas and Meneveau[25] ran the simulations for all choices of the kernel width with the same very high grid resolution. In their study, even the smallest kernel width $\epsilon/c = 0.25$ corresponded to a relative resolution of $\epsilon/\Delta x \approx 13$. In the present study, we choose to follow another approach since the application of FALM for full wind turbine rotors involves significantly smaller ratios $\epsilon/\Delta x < 5$. Otherwise, the advantage of the FALM, which is to enable coarser grid resolutions, would be lost. Instead, we choose to study the convergence of the results for lift coefficient and subfilter velocity correction on two coarser grids for each kernel width ϵ/c.

Figure 8 shows the magnitude of the subfilter correction $|\overline{\Delta u}_{ind}|$ along the span of the wing. Large magnitudes are limited to the proximity of the wing tips where the correction is needed to add the missing downwash, which is not resolved by LES due to a suboptimal kernel width $\epsilon^{LES} > \epsilon^{Opt}$. While for kernel widths of $\epsilon/c = \{1;2\}$, the correction is essentially zero in the midsection of the wing, the largest width $\epsilon/c = 4$

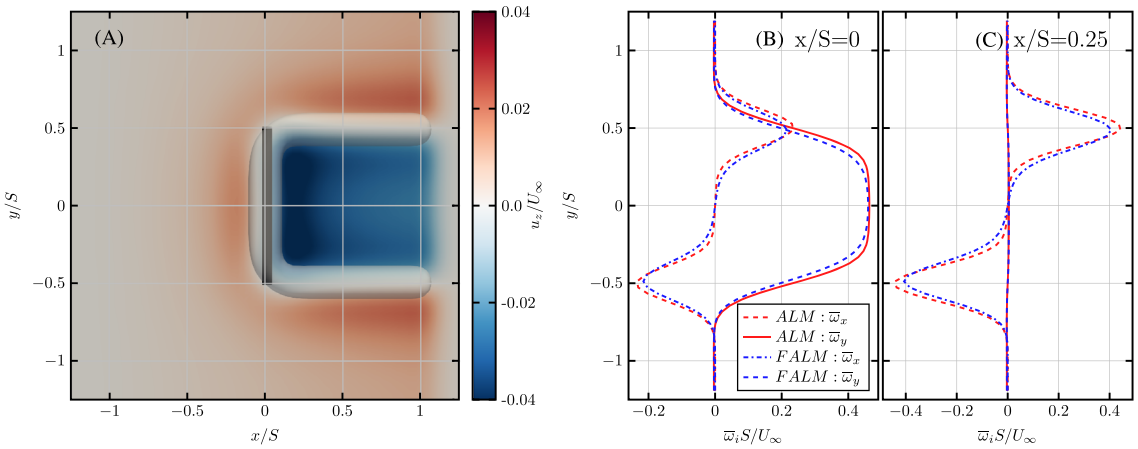

FIGURE 7 Vertical velocity field u_z/U_∞ and isosurface of the nondimensional vorticity magnitude $\overline{(\omega_i\omega_i)}^{1/2} S/U_\infty \approx 0.31$ around the translating wing used for testing of the FALM implementation (A). Comparison of the streamwise vorticity ω_x and lateral vorticity ω_y at the wing location $x/S = 0$ (B) and in the wake $x/S = 0.25$ (C) as obtained with the actuator line model (ALM) and filtered actuator line model (FALM). All the results are obtained for the parameter choice $\epsilon/c = 2$ and $\epsilon/\Delta x = 4$.

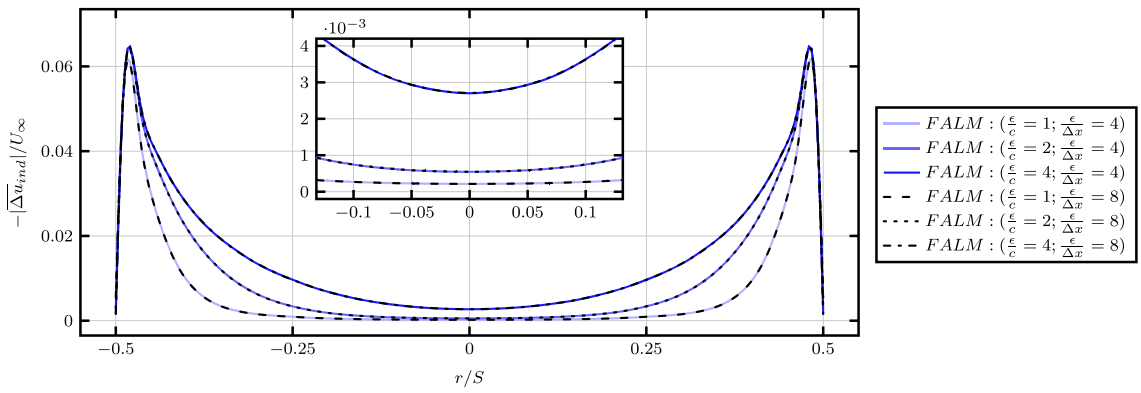

FIGURE 8 Convergence of the magnitude of the filtered actuator line model (FALM) subfilter correction $|\overline{\Delta u}_{ind}|$ along the span of the wing for different kernel widths ϵ/c.

requires a correction of the results for all spanwise locations. The amount of downwash resolved by the LES increases with decreasing LES kernel width, thus leading to a lowered magnitude of the subfilter correction along the entire span of the wing. As can be seen in the inset of Figure 8, the subfilter correction is already converged for a grid resolution of $\epsilon/\Delta x = 4$ for all three choices of the kernel width $\epsilon/c = \{1;2;4\}$. This finding is in agreement with previous results, which reported that convergence of the solution can be expected for grid resolutions of $\epsilon/\Delta x > 2.8$.[25]

The corresponding convergence behavior of the lift coefficient C_L is shown in Figure 9 for both the ALM and FALM, where the additional black dots denote the ALM reference solution obtained for $\epsilon^{LES} = \epsilon^{Opt} = 0.25c$ (taken from Martínez-Tossas and Meneveau[25]). In general, the lift distributions obtained with both models already indicate convergence for the coarser grid resolution of $\epsilon/\Delta x = 4$ for all three choices of ϵ/c. It is noted though that convergence is slightly slower for smaller kernel widths. This delay can be observed most clearly for the ALM results obtained with $\epsilon/c = 1$ in the region of the two local minima of the lift distribution.

The behavior of the FALM is now studied explicitly for the results obtained with $\epsilon/\Delta x = 8$. Figure 10 shows the resolved induced velocity $|\bar{u}_{ind}^{LES}|$ and the subfilter correction $|\overline{\Delta u}_{ind}|$ for varying kernel widths. Smaller LES kernel widths ϵ^{LES} lead to larger lift gradients at the tip (see Figure 9), which in turn create stronger tip vortices. The consequences are stronger-induced velocities along the wing span, especially in the proximity of the tip. In contrast, a wide kernel of $\epsilon/c = 4$ is insufficient to resolve the peaks in downwash close to the tips. It leads to a monotonous distribution of the downwash with respect to the half-wing length only showing one maximum at the wing center. Furthermore, the distribution of optimal-induced downwash $|\bar{u}_{ind}^{Opt}|$ does not depend on the LES kernel width ϵ^{LES}. Therefore, smaller LES kernel widths require a smaller subfilter correction, as is to be expected. The main benefit of the FALM is clearly visible in Figure 9. Even the smallest of the three studied kernel widths

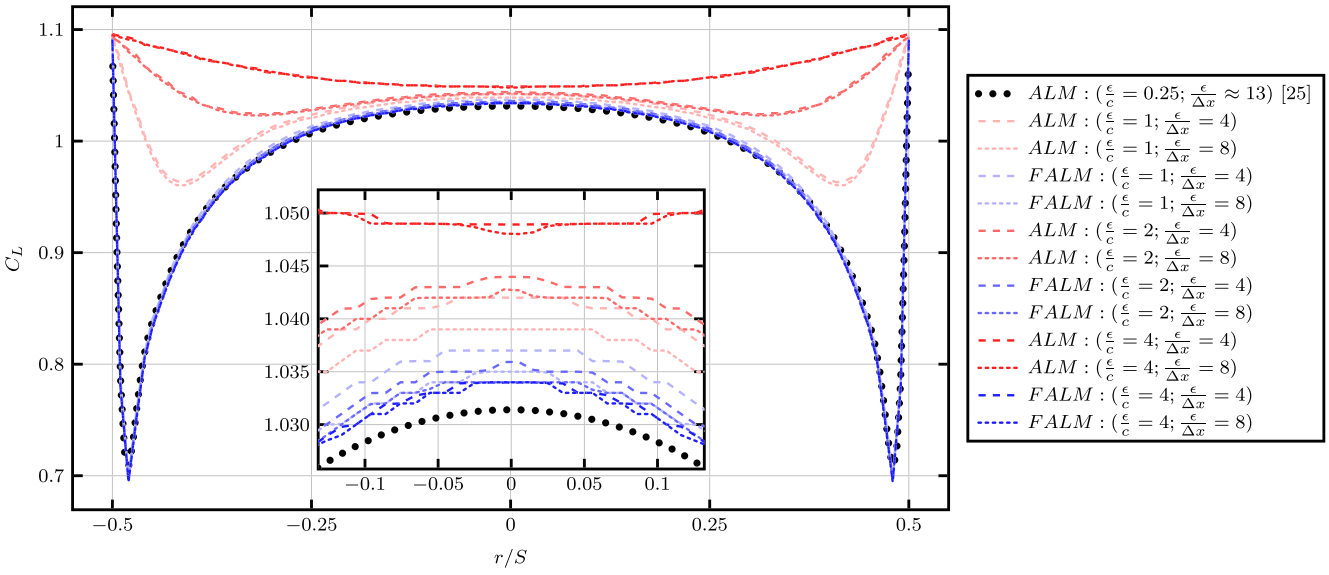

FIGURE 9 Convergence of the lift coefficient C_L along the span of the wing for different kernel widths ϵ/c using both actuator line model (ALM) and filtered actuator line model (FALM). The black dots denote the ALM reference solution obtained for $\epsilon^{LES} = \epsilon^{Opt} = 0.25c$ (taken from Martínez-Tossas and Meneveau[25]).

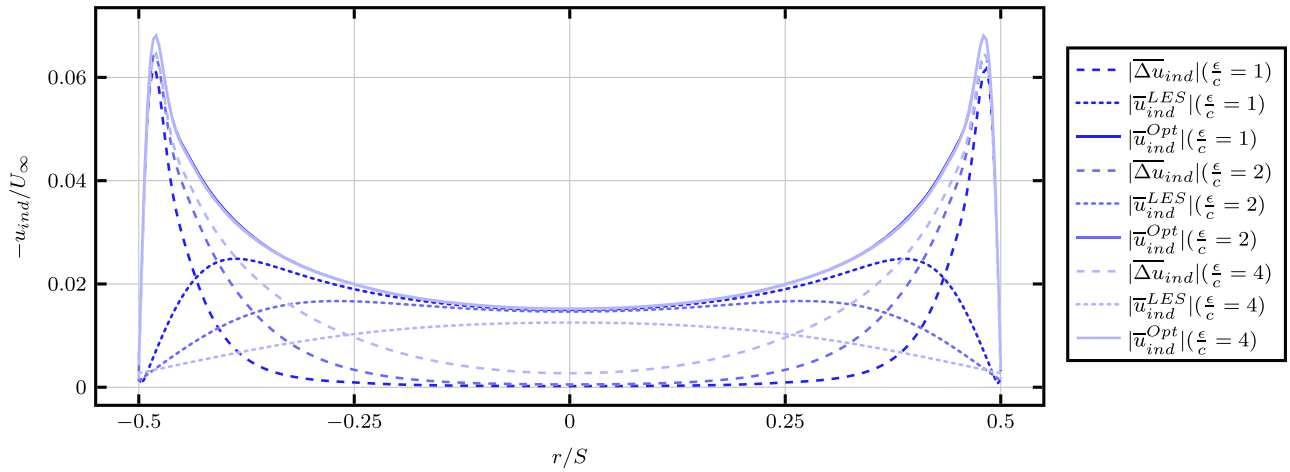

FIGURE 10 Dependence of the induced velocities u_{ind} on the kernel width ϵ/c for a grid resolution of $\epsilon/\Delta x = 8$.

exceeds the optimal value of $\epsilon^{Opt}/c = 0.25$ by a factor of 4. As a result, the lift distribution along the wing span varies strongly with the LES kernel width when using the ALM without correction. Further, the lift is significantly overpredicted near the tips due to underpredicted downwash. In contrast, the FALM captures the strong decrease in lift near the tips and importantly displays a solution that is independent of kernel width even for kernel widths exceeding the optimum value by a factor of 16. The epsilon-independent solution further matches the reference ALM lift profile obtained with ϵ^{Opt}. At this point, it should be noted that the performance of the FALM relies on the numerically calculated lift gradient (recall Equation (18)). An accurate calculation of the gradient is only possible with a large number of actuator points. For the present wing test case, a value of $N_F = 300$ is found to be necessary to obtain the correct magnitude and shape of the lift profiles. This undesirable effect could be at least partially compensated for by using a nonuniform actuator point spacing with high resolution only in the proximity of the wing tips.

4.3 | FALM versus ALM: NREL 5-MW turbine

After testing the implementation of the FALM with the translating wing example, its performance for a wind turbine is now compared with the ALM. The studied case is identical to the one used for the cross-verification of the ALM, that is, the NREL 5-MW reference turbine in uniform inflow (case parameters are shown in Section 3.3). Both ALM and FALM simulations are carried out for $\epsilon/D = \{0.079; 0.11\}$ while maintaining a grid resolution of $\epsilon/\Delta x = 3$ for each case. The aim is to study the differences in blade quantities and wake behavior for these larger Gaussian spreading widths and coarser grids since they are of practical importance when simulating an entire wind farm but also cause a significant overprediction of the generated power if no additional correction like the FALM is employed.[57] For the present comparison, both models use $N_F = N_V = 307$ to eliminate any possible influence of the number of actuator points. However, the required number of actuator points for the ALM and FALM are in general different and it is referred to Appendix C for a detailed convergence study.

The FALM computes a subfilter correction added to the sampled LES velocity based on the optimal-induced velocity and its resolved part along the blade. The mean profiles of these three velocities are shown in Figure 11. As observed in the previous section for the translating wing, large magnitudes of the induced velocities are limited to the inner and outer parts of the blade where the root and tip vortices cause strong induction. In the middle section of the blade, the coarse resolution and large spreading widths are sufficient to resolve the major share of the induced velocities, whereas toward the tip, the ratio of optimal and resolved induced velocity attains a ratio as large as $|\bar{u}_{ind}^{Opt}|/|\bar{u}_{ind}^{LES}| \approx 12$. The smaller Gaussian spreading $\epsilon/D = 0.079$ results in larger resolved induced velocity, especially in the interval $r/R = (0.7, 0.9)$ but still relies strongly on the subfilter correction in order to obtain the optimal downwash distribution. Further, it should be noted that the inflection points visible in the profiles of the correction and the optimal velocity are due to the discontinuities of the lift force distribution caused by the sudden changes of the airfoil type along the blade (see right center panel in Figure 12). The lift force profile also explains the sign change of the optimal-induced velocity at $r/R \approx 0.16$. The inner part of the blade of the NREL 5-MW turbine ($r/R < 0.16$) consists of circular airfoils, which do not provide any lift. Therefore, the positive velocity correction found close to the blade root is the upwash induced by the shed vorticity in the proximity of the strong lift gradient at $r/R \approx 0.16$.

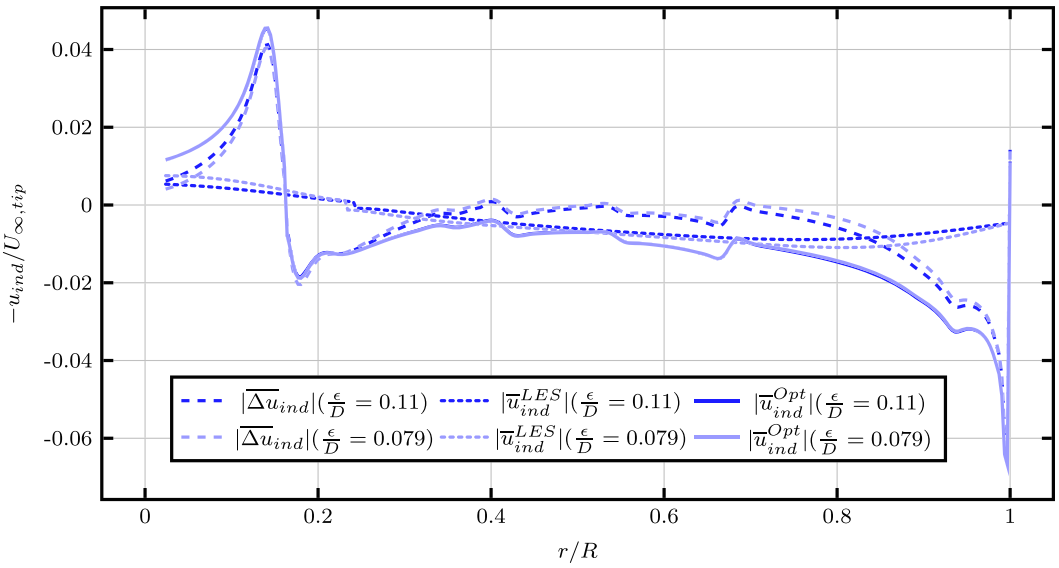

FIGURE 11 Magnitudes of the induced velocities u_{ind} along the blade span of the NREL 5-MW turbine shown for two different Gaussian kernel widths. All velocities are normalized with the magnitude of the unperturbed incoming velocity at the blade tip $U_{\infty,tip}$. The signs are determined by computing the alignment with respect to the lift force.

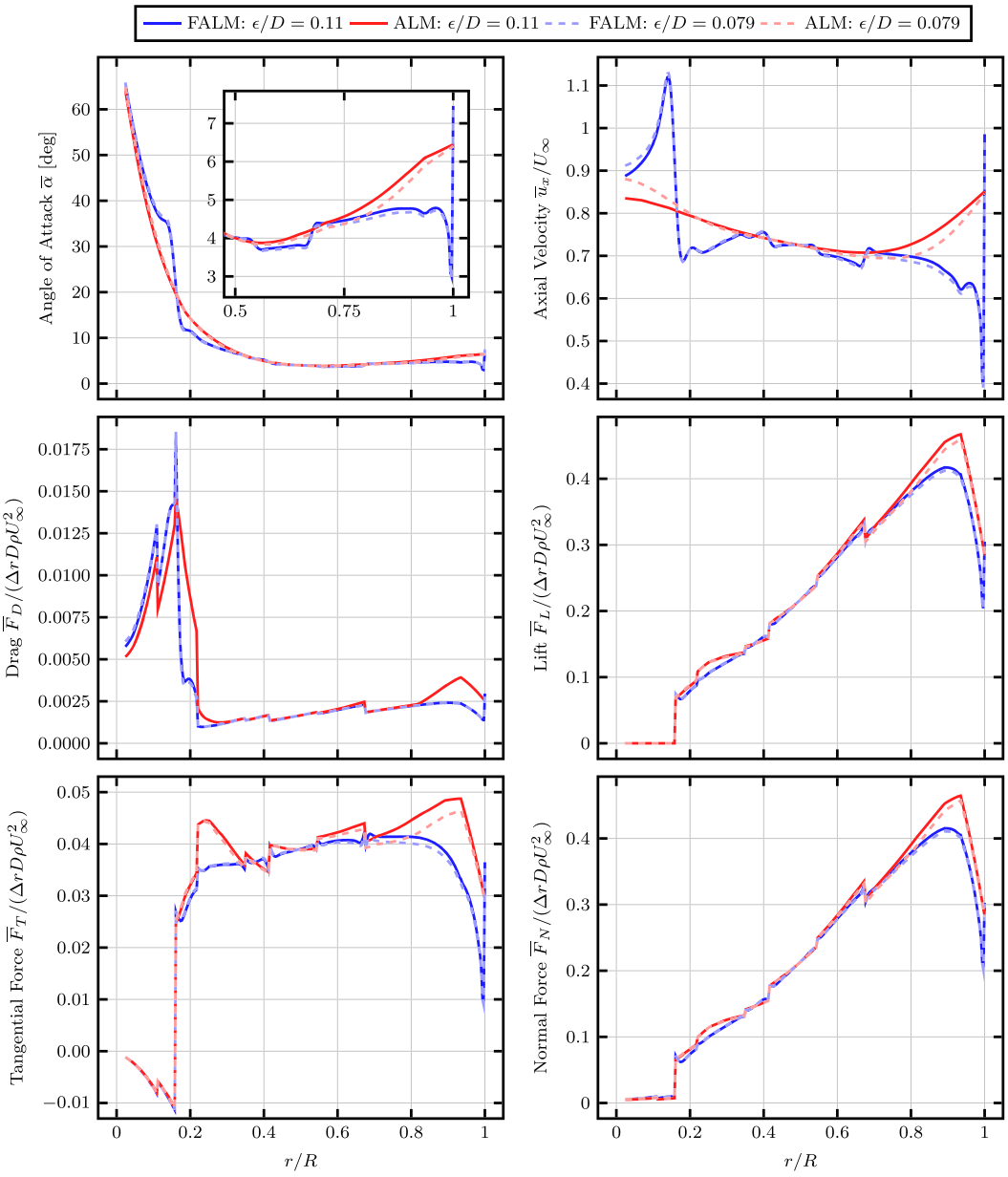

FIGURE 12 Actuator line model (ALM) versus filtered actuator line model (FALM): comparison of mean angle of attack $\overline{\alpha}$, axial velocity $\bar{u}_x/U_\infty$, drag, lift, tangential, and normal force per unit length along the blade span. The forces are nondimensionalized in the same manner as done for the ALM results (see Section 4.1).

The resulting profiles of angle of attack, axial velocity, and forces along the blade are presented in Figure 12. It is important to note that for this section, the second possible approach to obtain the blade specifications at the tip is employed, illustrating its impact on the results (data are now extrapolated from the two neighboring inner blade points instead of interpolated based on a zero chord assumption).

This user choice modifies the lift profile at the blade tip. It is important to keep this source of possible deviations between different ALM implementations in mind (compare with the other approach shown in Figure 2). As can be seen in the inset shown in the top left corner of Figure 12, the FALM correction results in a reduced angle of attack for $r/R > 0.75$. This change, in turn, leads to a lower lift force, which translates to reduced tangential and normal forces, ultimately decreasing the generated torque/power and thrust force. This finding is confirmed quantitatively in Table 4 where comparisons of ALM and FALM predictions for the rotor's thrust coefficient C_T and aerodynamic power coefficient C_P are shown. From the force profiles as well as the integral rotor quantities, it can be concluded that the FALM is successful in reducing the dependence of the solution on the width of the Gaussian spreading on coarse grids but cannot provide a fully independent solution (in terms of ϵ and Δx). This finding is confirmed by the study of Blaylock et al[27] who compared the dependence of the FALM solution on varying coarse meshes using a resolution of $\epsilon/\Delta x = 2$ instead of the $\epsilon/\Delta x = 3$ employed in this study. We expect that increasing $\epsilon/\Delta x$ would lead to improved convergence.

TABLE 4 Comparison of ALM and FALM predictions for the aerodynamic power and thrust coefficients of the NREL 5-MW rotor.

Power		Thrust	
$C_P(\epsilon/D=0.079)$ [-]	$100*\left(\frac{C_P(\epsilon/D=0.11)}{C_P(\epsilon/D=0.079)}-1\right)$ [%]	$C_T(\epsilon/D=0.079)$ [-]	$100*\left(\frac{C_T(\epsilon/D=0.11)}{C_T(\epsilon/D=0.079)}-1\right)$ [%]
ALM: 0.569	ALM: +3.51%	ALM: 0.838	ALM: +1.31%
FALM: 0.514	FALM: +1.56%	FALM: 0.805	FALM: +0.50%

Note: For both models absolute values are shown for $\epsilon/D=0.079$ and in addition relative increases for the coarser $\epsilon/D=0.11$.
Abbreviations: ALM, actuator line model; FALM, filtered actuator line model.

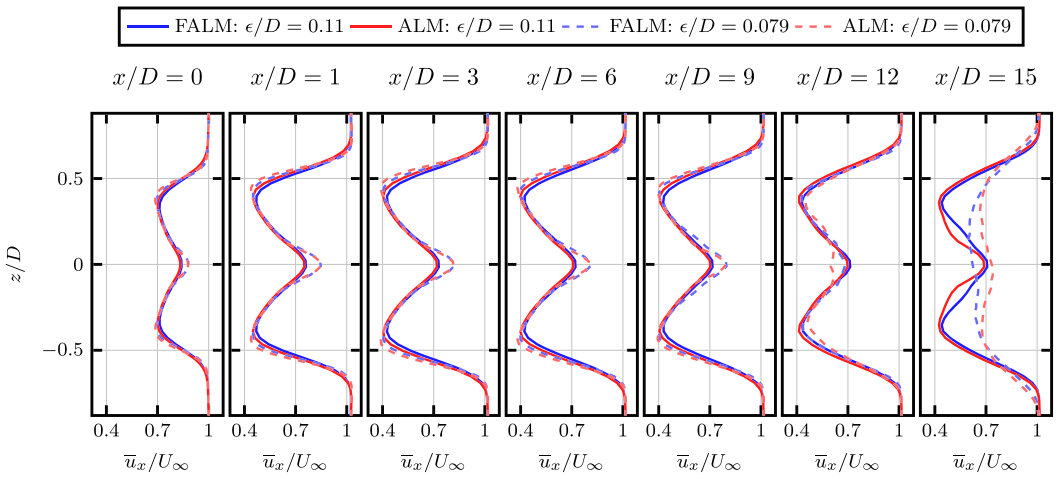

FIGURE 13 Actuator line model (ALM) versus filtered actuator line model (FALM): comparison of mean streamwise velocity profiles $\bar{u}_x/U_\infty$ at seven locations in the wake downstream of the turbine.

Furthermore, it should be noted that the preceding analysis focused on the modeling error inherent to the ALM for different ϵ^{LES} rather than comparing the error with another model like the blade element momentum (BEM) model which relies on very different simplifying assumptions. This focus is motivated by the fact that the FALM aims to correct the ALM results toward the mathematical solution of the underlying model equations solved for the optimal ϵ^{Opt} and thus its effectiveness should be judged in this context.

We conclude this study with an assessment of how the wake development is influenced by the application of the FALM. In Figure 13, mean streamwise velocity profiles are shown in the wake downstream of the turbine ranging from $x/D=0$ to $x/D=15$. It is possible to identify two main trends. Firstly, the wake is more stable for the case of larger spreading width $\epsilon/D=0.11$. In fact, the first signs of wake recovery are only visible for the location furthest downstream at $x/D=15$. This is likely to be caused by the smaller gradient of the shear layer, which is smoothed out by the larger width of the Gaussian spreading. In addition, the coarser resolution associated with this case delays the onset of transition as discussed in Section 4.1. Secondly, even for the same choices of ϵ and $\epsilon/\Delta x$ the wake differs between ALM and FALM. The reduced normal loading of the blades when using the FALM leads to both less induction and a less steep shear layer in the rotor plane at $x/D=0$. As a result, the application of the FALM delays the laminar-turbulent transition for both choices of ϵ. This conclusion is limited to laminar inflow scenarios, and further investigations are necessary to determine whether this finding holds true for turbulent inflow.

5 | CONCLUSIONS

The objective of this work was the development and subsequent verification of a new simulation environment that can give combined insights into the respective dynamics of the flow and individual turbines in a wind farm. Such an environment could then be further utilized to develop new dynamic wind farm control strategies, which require simultaneous knowledge about the development of the turbine wakes, the loads acting on the turbines, and the generated power. Additionally, the new environment should enable the use of GPU computing resources.

This aim was achieved by developing a new coupling between the GPU-resident LES code GRASP and the multiphysics turbine simulation tool OpenFAST. The coupling was implemented via an ALM and optionally offers the FALM extension. The ALM implementation was cross-verified with four other popular research LES codes with an ALM by comparing their performance in terms of blade and wake quantities for the

NREL 5-MW turbine in uniform inflow. The new coupling predicted similar results for the lift/drag forces along the blade and showed a good agreement for the near wake behavior when compared with the other four codes, thus confirming a successful implementation of the new ALM. Differences were found for the far wake development predicted by GRASP—in particular, the magnitude of the Reynolds stresses was lower than for the four references, and the mean streamwise velocity showed a slight asymmetry. The former finding was attributed to the coarser grid resolution used for GRASP compared with the references, whereas the latter was expected to be caused by the limitation that GRASP currently does not offer a slip wall BC for the bottom boundary. The implementation of the FALM was tested with a simple translating wing, and its performance was subsequently compared with the ALM for the NREL 5-MW turbine. The FALM proved to be successful in reducing the dependence of the blade loads and the generated power on the width of the Gaussian kernel used to project the point forces onto the LES grid. Furthermore, the wake predicted with the FALM was shown to transition later than for the traditional ALM when considering uniform inflow.

Future work will be oriented toward two objectives. Firstly, the development of a multi-GPU version of GRASP can enable the study of cases with larger domains and higher resolution. Secondly, the new simulation environment can be utilized to study new wind farm control strategies including the turbulent ABL.

ACKNOWLEDGEMENTS

This work is part of the Hollandse Kust Noord wind farm innovation program where CrossWind C.V., Shell, Eneco, and Siemens Gamesa are teaming up; funding for the PhDs was provided by CrossWind C.V. and Siemens Gamesa. This work was authored in part by the National Renewable Energy Laboratory, operated by the Alliance for Sustainable Energy, LLC, for the US Department of Energy (DOE) under contract no. DE-AC36-08GO28308. Funding was provided by the US Department of Energy Office of Energy Efficiency and Renewable Energy Wind Energy Technologies Office. The views expressed in the article do not necessarily represent the views of the DOE or the US Government. The US Government retains and the publisher, by accepting the article for publication, acknowledges that the US Government retains a nonexclusive, paid-up, irrevocable, worldwide license to publish or reproduce the published form of this work or allow others to do so, for US Government purposes.

CONFLICT OF INTEREST STATEMENT

The authors declare no potential conflict of interests.

DATA AVAILABILITY STATEMENT

The data that support the findings of this study are available from the corresponding author upon reasonable request.

ORCID

Emanuel Taschner https://orcid.org/0000-0002-0296-8168
Luis A Martínez-Tossas https://orcid.org/0000-0003-2353-4999
Jan-Willem van Wingerden https://orcid.org/0000-0003-3061-7442

REFERENCES

1. Hansen AC, Butterfield CP. Aerodynamics of horizontal-axis wind turbines. *Annu Rev Fluid Mech*. 1993;25(1):115-149. https://doi.org/10.1146/annurev.fl.25.010193.000555
2. Sørensen JN. Aerodynamic aspects of wind energy conversion. *Annu Rev Fluid Mech*. 2011;43(1):427-448. https://doi.org/10.1146/annurev-fluid-122109-160801
3. Veers P, Dykes K, Lantz E, et al. Grand challenges in the science of wind energy. *Science*. 2019;366(6464):eaau2027. https://doi.org/10.1126/science.aau2027
4. Stevens RJ, Meneveau C. Flow structure and turbulence in wind farms. *Annu Rev Fluid Mech*. 2017;49(1):311-339. https://doi.org/10.1146/annurev-fluid-010816-060206
5. Porté-Agel F, Bastankhah M, Shamsoddin S. Wind-turbine and wind-farm flows: a review. *Bound-Layer Meteorol*. 2020;174(1):1-59. https://doi.org/10.1007/s10546-019-00473-0
6. Bossanyi EA. Wind turbine control for load reduction. *Wind Energy*. 2003;6(3):229-244. https://doi.org/10.1002/we.95
7. Andersson LE, Anaya-Lara O, Tande JO, Merz KO, Imsland L. Wind farm control—part I: a review on control system concepts and structures. *IET Renew Power Gener*. 2021;15(10):2085-2108. https://doi.org/10.1049/rpg2.12160
8. Meyers J, Bottasso C, Dykes K, et al. Wind farm flow control: prospects and challenges. *Wind Energy Sci Discuss*. 2022;7:2271-2306. https://doi.org/10.5194/wes-2022-24
9. Goit JP, Meyers J. Optimal control of energy extraction in wind-farm boundary layers. *J Fluid Mech*. 2015;768:5-50. https://doi.org/10.1017/jfm.2015.70
10. van der Hoek D, Frederik J, Huang M, Scarano F, Simao Ferreira C, van Wingerden J-W. Experimental analysis of the effect of dynamic induction control on a wind turbine wake. *Wind Energy Sci*. 2022;7(3):1305-1320. https://doi.org/10.5194/wes-7-1305-2022
11. Frederik JA, Doekemeijer BM, Mulders SP, van Wingerden J-W. The helix approach: using dynamic individual pitch control to enhance wake mixing in wind farms. *Wind Energy*. 2020;23(8):1739-1751. https://doi.org/10.1002/we.2513
12. Frederik JA, van Wingerden J-W. On the load impact of dynamic wind farm wake mixing strategies. *Renew Energy*. 2022;194:582-595. https://doi.org/10.1016/j.renene.2022.05.110

13. Calaf M, Meneveau C, Meyers J. Large eddy simulation study of fully developed wind-turbine array boundary layers. *Phys Fluids*. 2010;22(1):15110. https://doi.org/10.1063/1.3291077
14. Lu H, Porté-Agel F. Large-eddy simulation of a very large wind farm in a stable atmospheric boundary layer. *Phys Fluids*. 2011;23(6):65101. https://doi.org/10.1063/1.3589857
15. Pope S. *Turbulent Flows*: Cambridge University Press; 2001.
16. Sanderse B, Pijl SP, Koren B. Review of computational fluid dynamics for wind turbine wake aerodynamics: review of CFD for wind turbine wake aerodynamics. *Wind Energy*. 2011;14(7):799-819. https://doi.org/10.1002/we.458
17. Mehta D, van Zuijlen AH, Koren B, Holierhoek JG, Bijl H. Large eddy simulation of wind farm aerodynamics: a review. *J Wind Eng Ind Aerodyn*. 2014;133:1-17. https://doi.org/10.1016/j.jweia.2014.07.002
18. Sorensen JN, Shen WZ. Numerical modeling of wind turbine wakes. *J Fluids Eng*. 2002;124(2):393-399. https://doi.org/10.1115/1.1471361
19. Troldborg N, Sorensen JN, Mikkelsen R. Numerical simulations of wake characteristics of a wind turbine in uniform inflow. *Wind Energy*. 2010;13(1):86-99. https://doi.org/10.1002/we.345
20. Churchfield MJ, Schreck SJ, Martinez LA, Meneveau C, Spalart PR. An advanced actuator line method for wind energy applications and beyond. In: American Institute of Aeronautics and Astronautics; 2017; Grapevine, Texas. https://doi.org/10.2514/6.2017-1998
21. Martínez-Tossas LA, Churchfield MJ, Meneveau C. Optimal smoothing length scale for actuator line models of wind turbine blades based on Gaussian body force distribution. *Wind Energy*. 2017;20(6):1083-1096. https://doi.org/10.1002/we.2081
22. Meyer Forsting AR, Pirrung GR, Ramos-García N. A vortex-based tip/smearing correction for the actuator line. *Wind Energy Sci*. 2019;4(2):369-383. https://doi.org/10.5194/wes-4-369-2019
23. Dağ KO, Sørensen JN. A new tip correction for actuator line computations. *Wind Energy*. 2020;23(2):148-160. https://doi.org/10.1002/we.2419
24. Kleine VG, Hanifi A, Henningson DS. Non-iterative smearing correction for the actuator line method. Tech. Rep. arXiv:2206.05448, arXiv; 2022. arXiv:2206.05448 [physics] type: article.
25. Martínez-Tossas LA, Meneveau C. Filtered lifting line theory and application to the actuator line model. *J Fluid Mech*. 2019;863:269-292. https://doi.org/10.1017/jfm.2018.994
26. Stanly R, Martínez-Tossas LA, Frankel SH, Delorme Y. Large-eddy simulation of a wind turbine using a filtered actuator line model. *J Wind Eng Ind Aerodyn*. 2022;222:104868. https://doi.org/10.1016/j.jweia.2021.104868
27. Blaylock ML, Martinez-Tossas L, Sakievich P, et al. Validation of actuator line and actuator disk models with filtered lifting line corrections implemented in Nalu-Wind large eddy simulations of the atmospheric boundary layer. In: American Institute of Aeronautics and Astronautics; 2022; San Diego, CA & Virtual. https://doi.org/10.2514/6.2022-1921
28. Jonkman J. The new modularization framework for the FAST wind turbine CAE tool. In: American Institute of Aeronautics and Astronautics; 2013; Grapevine (Dallas/Ft.Worth Region), Texas.
29. Larsen TJ, Hansen AM. How 2 HAWC2 the user's manual. *Technical Report Risø-R-1597(ver. 12.7)(EN)*, Denmark, Risø National Laboratory for Sustainable Energy; 2019.
30. Abbas NJ, Zalkind DS, Pao L, Wright A. A reference open-source controller for fixed and floating offshore wind turbines. *Wind Energy Sci*. 2022;7(1):53-73. https://doi.org/10.5194/wes-7-53-2022
31. Storey RC, Norris SE, Stol KA, Cater JE. Large eddy simulation of dynamically controlled wind turbines in an offshore environment. *Wind Energy*. 2013;16(6):845-864. https://doi.org/10.1002/we.1525
32. Churchfield MJ, Lee S, Michalakes J, Moriarty PJ. A numerical study of the effects of atmospheric and wake turbulence on wind turbine dynamics. *J Turbul*. 2012;13:N14. https://doi.org/10.1080/14685248.2012.668191
33. Storey RC, Norris SE, Cater JE. An actuator sector method for efficient transient wind turbine simulation. *Wind Energy*. 2015;18(4):699-711. https://doi.org/10.1002/we.1722
34. Heinz JC, Sørensen NN, Zahle F. Fluid-structure interaction computations for geometrically resolved rotor simulations using CFD: fluid-structure interaction computations for geometrically resolved rotor simulations using CFD. *Wind Energy*. 2016;19(12):2205-2221. https://doi.org/10.1002/we.1976
35. Krüger S, Steinfeld G, Kraft M, Lukassen LJ. Validation of a coupled atmospheric-aeroelastic model system for wind turbine power and load calculations. *Wind Energy Sci*. 2022;7(1):323-344. https://doi.org/10.5194/wes-7-323-2022
36. Sprague MA, Boldyrev S, Fischer P, Grout R, Gustafson WI, Moser R. Turbulent flow simulation at the exascale: opportunities and challenges workshop. *Tech. Rep. NREL/TP-2C00-67648*. 1338668, Washington, D.C., U.S. Department of Energy, Office of Science, Advanced Scientific Computing Research; 2015.
37. Sprague MA, Ananthan S, Vijayakumar G, Robinson M. ExaWind: a multifidelity modeling and simulation environment for wind energy. *J Phys Conf Ser*. 2020;1452(1):12071. https://doi.org/10.1088/1742-6596/1452/1/012071
38. Heus T, van Heerwaarden CC, Jonker HJJ, et al. Formulation of the Dutch atmospheric large-eddy simulation (DALES) and overview of its applications. *Geosci Model Dev*. 2010;3(2):415-444. https://doi.org/10.5194/gmd-3-415-2010
39. Schalkwijk J, Griffith EJ, Post FH, Jonker HJJ. High-performance simulations of turbulent clouds on a desktop PC: exploiting the GPU. *Bull Am Meteorol Soc*. 2012;93(3):307-314. https://doi.org/10.1175/BAMS-D-11-00059.1
40. Schalkwijk J, Jonker HJJ, Siebesma AP, Van Meijgaard E. Weather forecasting using GPU-based large-eddy simulations. *Bull Am Meteorol Soc*. 2015;96(5):715-723. https://doi.org/10.1175/BAMS-D-14-00114.1
41. Böing SJ, Jonker HJJ, Siebesma AP, Grabowski WW. Influence of the subcloud layer on the development of a deep convective ensemble. *J Atmos Sci*. 2012;69(9):2682-2698. https://doi.org/10.1175/JAS-D-11-0317.1
42. Smagorinsky J. General circulation experiments with the primitive equations: I. The basic experiment. *Mon Weather Rev*. 1963;91(3):99-164. https://doi.org/10.1175/1520-0493(1963)091<0099:GCEWTP>2.3.CO;2
43. Wicker LJ, Skamarock WC. Time-splitting methods for elastic models using forward time schemes. *Mon Weather Rev*. 2002;130(8):2088-2097. https://doi.org/10.1175/1520-0493(2002)130<2088:TSMFEM>2.0.CO;2
44. Gilbert C, Messner JW, Pinson P, Trombe PJ, Verzijlbergh R, Dorp P, Jonker H. Statistical post-processing of turbulence-resolving weather forecasts for offshore wind power forecasting. *Wind Energy*. 2020;23(4):884-897. https://doi.org/10.1002/we.2456
45. Schepers G, van Dorp P, Verzijlbergh R, Baas P, Jonker H. Aeroelastic loads on a 10 MW turbine exposed to extreme events selected from a year-long large-eddy simulation over the North Sea. *Wind Energy Sci*. 2021;6(4):983-996. https://doi.org/10.5194/wes-6-983-2021

46. Schalkwijk J, Jonker HJJ, Siebesma AP, Bosveld FC. A year-long large-eddy simulation of the weather over Cabauw: an overview. *Mon Weather Rev*. 2015;143(3):828-844. Publisher: American Meteorological Society Section: Monthly Weather Review doi:10.1175/MWRD-14-00293.1.
47. Vollmer L, Steinfeld G, Kühn M. Transient LES of an offshore wind turbine. *Wind Energy Sci*. 2017;2(2):603-614. https://doi.org/10.5194/wes-2-603-2017
48. Santoni C, García-Cartagena EJ, Ciri U, Zhan L, Valerio Iungo G, Leonardi S. One-way mesoscale-microscale coupling for simulating a wind farm in North Texas: assessment against SCADA and LiDAR data. *Wind Energy*. 2020;23(3):691-710. https://doi.org/10.1002/we.2452
49. OpenFAST/openfast at v3.0.0, Available online at: https://github.com/OpenFAST/openfast/tree/v3.0.0
50. Jonkman JM, Hayman GJ, Jonkman BJ, Damiani RR, Murray RE. AeroDyn v15 user's guide and theory manual, Golden, Colorado, USA, NREL; 2017.
51. Santoni C, Carrasquillo K, Arenas-Navarro I, Leonardi S. Effect of tower and nacelle on the flow past a wind turbine: effect of tower and nacelle on the flow past a wind turbine. *Wind Energy*. 2017;20(12):1927-1939. https://doi.org/10.1002/we.2130
52. Gao Z, Li Y, Wang T, Shen W, Zheng X, Prösting S, Li D, Li R. Modelling the nacelle wake of a horizontal-axis wind turbine under different yaw conditions. *Renew Energy*. 2021;172:263-275. https://doi.org/10.1016/j.renene.2021.02.140
53. Martínez-Tossas LA, Churchfield MJ, Yilmaz AE, Sarlak H, Johnson PL, Sørensen JN, Meyers J, Meneveau C. Comparison of four large-eddy simulation research codes and effects of model coefficient and inflow turbulence in actuator-line-based wind turbine modeling. *J Renew Sustain Energy*. 2018;10(3):33301. https://doi.org/10.1063/1.5004710
54. Jonkman J, Butterfield S, Musial W, Scott G. Definition of a 5-MW reference wind turbine for offshore system development. NREL/TP-500-38060, 947422; 2009.
55. Martínez-Tossas LA, Churchfield MJ, Leonardi S. Large eddy simulations of the flow past wind turbines: actuator line and disk modeling. *Wind Energy*. 2015;18(6):1047-1060. https://doi.org/10.1002/we.1747
56. Moin P, Verzicco R. On the suitability of second-order accurate discretizations for turbulent flow simulations. *Eur J Mech - B/Fluids*. 2016;55:242-245. https://doi.org/10.1016/j.euromechflu.2015.10.006
57. Stevens RJAM, Martínez-Tossas LA, Meneveau C. Comparison of wind farm large eddy simulations using actuator disk and actuator line models with wind tunnel experiments. *Renew Energy*. 2018;116:470-478. https://doi.org/10.1016/j.renene.2017.08.072

How to cite this article: Taschner E, Folkersma M, A Martínez-Tossas L, Verzijlbergh R, van Wingerden J-W. A new coupling of a GPU-resident large-eddy simulation code with a multiphysics wind turbine simulation tool. *Wind Energy*. 2024;27(11):1152-1172. doi:10.1002/we.2844

APPENDIX A: GRASP-OPENFAST COUPLING VIA THE (FILTERED) ALM

Algorithm 1

while $n < n_{tmax}$ **do**
  ASPIRE: Transfer LES velocity data from GPU to CPU
  for $m \leftarrow 1$ to N_{Blades} **do**
    for $k \leftarrow 1$ to $N_{V,F}$ **do**
      if FALM **then**
        AspFAST: Sample LES velocity at force actuator point
        AspFAST: Compute the new subgrid velocity correction: Equations 14, 15,16, 17, 18 and 19
        AspFAST: Correct the sampled LES velocity: Equation 20
        OpenFAST: Interpolate velocity from force to velocity actuator point
      else
        AspFAST: Sample LES velocity at velocity actuator point
      OpenFast: Compute velocity magnitude: Equation 5
      OpenFast: Compute angle of attack: Equations 6, 7
      OpenFast: Compute actuator point force: Equations 8, 9
      if FALM **then**
        AspFAST: Store actuator point force
  AspFAST: Project point forces onto LES grid: Equations 10, 11
  ASPIRE: Transfer the wind turbine body force data from CPU to GPU
  GRASP: Advance the governing LES equations (Equations 1 and 2) by one time step
  $n+ = 1$

APPENDIX B: PERFORMANCE ASSESSMENT

This appendix provides an overview of the computational speed associated with the different configurations of the new simulation environment. In particular, it is distinguished between three configurations: the LES code operating in isolation, the LES code coupled one-way to OpenFAST (only velocities are sampled from the LES and passed on), and the LES code coupled two-way to OpenFAST (exchange of velocites and forces). To this end, a test case based on the ALM cross-verification from Section 3.1 is designed considering three different grid resolutions ($\Delta x/D = 1/63, \Delta x/D = 2/63$, and $\Delta x/D = 4/63$), which results in a total of nine cases. The domain size is $L_x \times L_y \times L_z = (8.12D)^3$ with the turbine hub centered within the cubic domain. For all cases, the number of actuator points is kept constant as $N_F = N_V = 64$, and the ratio of Gaussian kernel width to grid spacing is fixed as $\epsilon/\Delta x = 2$. All nine cases are advanced for 3000 steps in time to collect robust wall time estimates. In addition, the wall time results from Section 3.1,3.3 and Appendix C are collected to present a complete overview of the computational performance in Figure B1. Simulations are performed on two different computing platforms: firstly, utilizing a single GPU node on an HPC cluster equipped with one NVIDIA A100-SXM4-40GB GPU and 12 Intel(R) Xeon(R) CPU @ 2.20GHz (abbreviated as A100 in B1) and secondly, utilizing a standalone GPU machine equipped with one NVIDIA GeForce RTX 3090-24GB GPU and a total availability of 64 Intel(R) Xeon(R) CPU E7-4809 v4 @ 2.10GHz (abbreviated as GTX in B1). It should be noted that the three large test cases using $\Delta x/D = 1/63$ are not permitted by the 24GB memory of the smaller GeForce RTX GPU. For the six cases permitted by both GPU memories, the single HPC node equipped with the A100 leads to better performance for all cases.

Furthermore, the differences between the different coupling configurations and the additional expense of the FALM can be assessed. The standalone LES code is approximately one order of magnitude faster than the two-way coupled code for the medium and large test cases. This is to be expected as the calculations performed by AspFAST and OpenFAST are both carried out on CPUs and also require additional data transfer between GPU and CPU. The one-way coupling only performs the sampling of the velocities at the actuator points and the OpenFAST internal calculations but does not require the projection of the body force onto the LES grid, which results in an approximately two times faster speed compared with the two-way coupling. The simulation from Section 3.1 (red square in Figure B1) does not reach the speed of the test case for two reasons: Firstly, the number of grid cells (N_x, N_y, N_z) are not integer powers of two, which leads to a suboptimal division of the problem on the GPU. Secondly, the $\epsilon/\Delta x$ ratio is equal to five rather than two which requires the projection of the body force onto more LES grid points (as the projection is only calculated for grid points where the strength of the Gaussian kernel η_ϵ is larger than 0.1% of its center value).

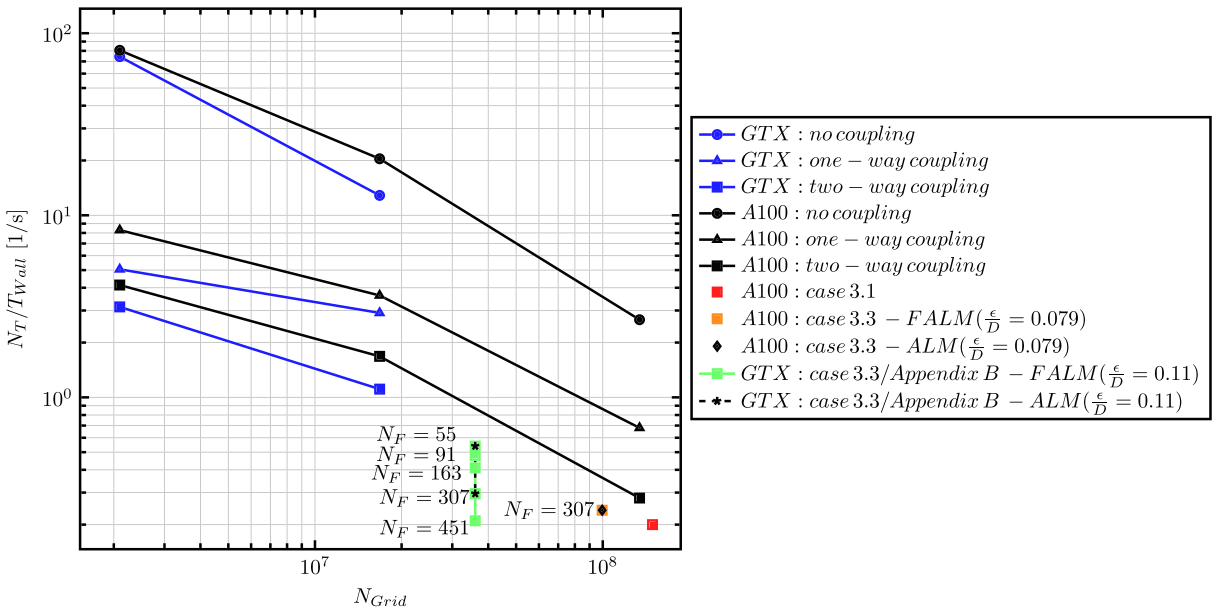

FIGURE B1 Scaling of the computational speed in terms of computed time steps per wall clock second with increasing problem size N_{Grid}. Results are shown for the standalone large-eddy simulation (LES) code (no coupling), one-way and two-way coupling. Furthermore, the results from Sections 3.1 and 3.3 and Appendix C are presented. The number of actuator points is $N_F = 64$ except if specifically noted otherwise in the plot next to the corresponding marker.

To conclude, the computational overhead added by the FALM is assessed. The additional computation of the subgrid velocity correction (Equations 14–20) is found to be negligible (black diamond matches orange square and black stars match the green squares in Figure B1). The added overhead is rather determined by the required number of actuator points N_F for the FALM. The convergence of the FALM results is studied in Appendix C concluding that at least $N_F = 150$ is required compared with well-converged ALM results with $N_F = 55$. The FALM with $N_F = 163$ reduces N_T/T_{Wall} by about 25% compared with the ALM with $N_F = 55$.

APPENDIX C: CONVERGENCE OF THE FALM RESULTS

The quality of the FALM results relies on the accurate calculation of both the resolved and optimal-induced velocity along the blade in Equation (18). The smallest length scales across which the resolved/optimal-induced velocities can vary are given by the widths of the Gaussian kernels ϵ^{LES} and ϵ^{Opt}, respectively. Since in general $\epsilon^{LES} \gg \epsilon^{Opt}$, the latter one imposes the requirement of finer actuator point spacing along the blade compared with the traditional ALM. This fact becomes apparent in Figure C2A where the convergence of the lift force near the blade tip is studied as function of the number of actuator points (using the FALM $\epsilon/D = 0.11$ case defined in Section 3.3). It can be seen that the FALM using $N_F = 55$ is incapable of predicting the sharp drop of the lift force at the blade tip due to the presence of the tip vortex. While the accurate prediction of the magnitude of this drop requires at least $N_F = 163$ points, full convergence of the lift profile is only obtained for $N_F \approx 300$. The aerodynamic power and thrust coefficients C_P and C_T of the rotor further confirm these findings (Figure C2B), where the percentage differences between the power and thrust coefficients obtained for $N_F = 55$ and $N_F = 307$ are $\approx 1.8\%$ and $\approx 0.7\%$. In contrast, the differences for the ALM are only $\approx 0.014\%$ and $\approx 0.011\%$ indicating convergence of the ALM results with $N_F = 55$.

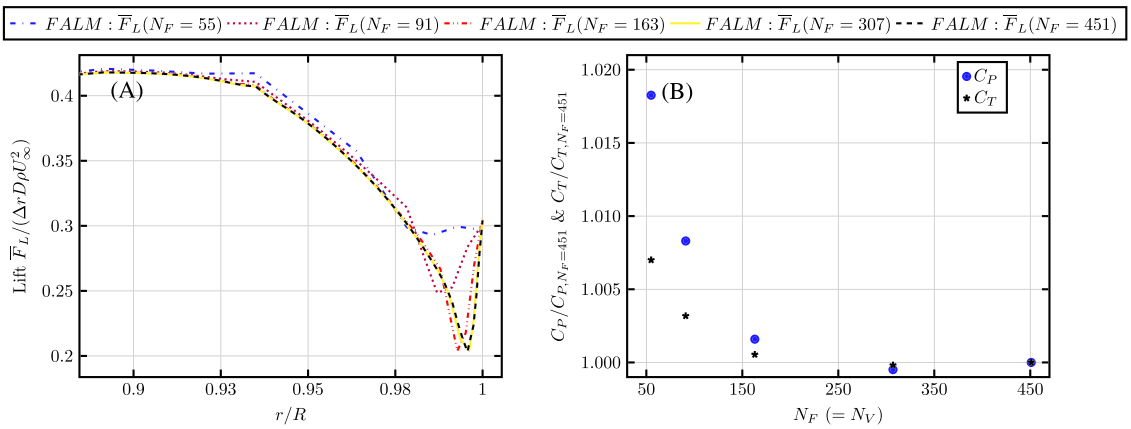

FIGURE C2 Convergence of the filtered actuator line model (FALM) results ($\epsilon/D = 0.11$) for the NREL 5-MW turbine with increasing number of actuator points ($N_F = N_V$) shown for the lift force per unit length in the outer region of the blade (A) and the aerodynamic thrust and power coefficients of the rotor normalized with their respective values obtained for $N_F = 451$ (B).